

Mesostructural origins of the anisotropic compressive properties of low-density closed-cell foams: A deeper understanding

L. Liu^{a,*}, F. Liu^a, D. Zenkert^b, M. Åkermo^b, M. Fagerström^a

^a*Department of Industrial and Materials Science, Chalmers University of Technology, SE-41296 Gothenburg, Sweden*

^b*Department of Engineering Mechanics, KTH Royal Institute of Technology, SE-10044 Stockholm, Sweden*

Abstract

Many closed-cell foams exhibit an elongated cell shape in the foam rise direction, resulting in anisotropic compressive properties, e.g. modulus and strength. Nevertheless, the underlying deformation mechanisms and how cell shape anisotropy induces this mechanical anisotropy are not yet fully understood, in particular for the foams with a high cell face fraction and low relative density. Moreover, the impacts of mesostructural stochastics are often overlooked.

This contribution conducts a systematic numerical study on the anisotropic compressive behaviour of low-density closed-cell foams, which accounts for cell shape anisotropy, cell structure and different mesostructural stochastics. Representative volume elements (RVE) of foam mesostructures are modeled, with cell walls described as Reissner-Mindlin shells in a finite rotation setting. A mixed stress-strain driven homogenization scheme is introduced, which allows for enforcing an overall uniaxial stress state. The base material behaviour is described using a stress resultant-based isotropic elastic model. Uniaxial compressive loadings in different global directions are applied.

Quantitative analysis of the cell wall deformation behavior confirms the dominant role of membrane deformation in the initial elastic region, while the bending contribution gets important only after foam yielding. Following the identified deformation mechanisms, analytical models are developed that relates mechanical anisotropy to cell shape anisotropy. It is found that cell shape anisotropy translates into the anisotropy of compressive properties through three pathways, cell load-bearing area fraction, cell wall buckling stress and cell wall inclination angle. Besides, the resulting mechanical anisotropy is strongly affected by the cell shape anisotropy stochastics while almost insensitive to the cell size and cell wall thickness stochastics. The present findings provide deeper insights into the relationships between the anisotropic compressive properties and mesostructural features of close-cell foams.

Keywords: Closed-cell foams, anisotropic compressive properties, cell shape anisotropy, stochastic variations, Laguerre tessellation, strain energy partitioning

1. Introduction

Closed-cell foams are widely utilized in modern engineering applications due to their appealing specific mechanical properties with respect to low density, e.g. high stiffness and strength, and great energy absorption capacity [1, 2, 3]. These properties are attributed to the underlying mesostructure, which typically consists of a large number of cells isolated

*Corresponding author.

Email address: lei.liu@chalmers.se (L. Liu)

Nomenclature

$\tilde{\mathbf{H}}^c, \vec{G}^c, \mathbf{K}^c$	Mesoscale shell membrane strain tensor, transverse shear strain vector and bending curvature tensor
$\tilde{\mathbf{N}}^c, \vec{V}^c, \mathbf{M}^c$	Mesoscale shell membrane stress resultant tensor, transverse shear stress resultant vector and bending moment tensor
$\hat{\mathbf{F}}$	Macroscale deformation gradient tensor
$\hat{\mathbf{P}}$	Macroscale first Piola-Kirchhoff stress tensor
$\hat{E}, \hat{\nu}, \hat{\sigma}_y$	Foam compressive modulus, Poisson's ratio and yield strength
\mathbf{F}	Mesoscale deformation gradient tensor
\mathbf{L}, \mathbf{K}	Mesoscale shell cross-sectional deformation gradient tensor and its through-thickness gradient
\mathbf{N}, \mathbf{M}	Mesoscale shell stress resultant tensor and couple-stress resultant tensor
\mathbf{P}	Mesoscale first Piola-Kirchhoff stress tensor
\mathcal{D}_w	Cell wall buckling occurrence detector
\mathcal{I}_w	Cell wall strain energy partitioning indicator
\mathcal{R}	Foam cell shape anisotropy
$\mathcal{R}^E, \mathcal{R}^\sigma$	Foam compressive modulus anisotropy and strength anisotropy
$\mathcal{R}_f, \mathcal{R}_c, \mathcal{R}_\theta$	Cell load-bearing area fraction ratio, cell wall buckling stress ratio and cell wall inclination angle ratio
\mathcal{R}_w	Cell wall aspect ratio
θ_w	Cell wall inclination angle
E, ν	Base material Young's modulus and Poisson's ratio
k_c	Cell wall buckling coefficient
$K_w, \sigma_{c,w}$	Cell wall membrane stiffness and buckling stress

by thin cell walls (see Figure 1). During the foaming process, cells tend to elongate in the foam rise direction, resulting in an anisotropic cell shape [4, 5]. Cell walls are usually thicker around the edges and thinner close to the face centers [6, 7], commonly described by the cell edge/face material partitioning [8]. Moreover, many mesostructural features, e.g. relative density, cell shape, cell size and cell wall thickness, are highly variable [6, 9]. All the above lead to a broad spectrum of mechanical properties.

Given the exploitation of closed-cell foams for load-bearing applications, the compressive behavior is often of interest [1, 2, 3]. For most elasto-plastic foams, the compressive stress-strain response can be divided into three regions: elasticity, plateau and densification [8]. The first region is governed by the elastic membrane (or stretching) and bending defor-

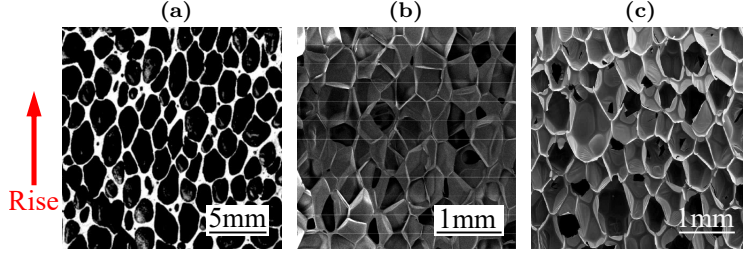


Figure 1: Examples of closed-cell foam mesostructures made from different base materials: (a) aluminium, (b) polyvinylchlorid (PVC) and (c) polyisocyanurate (PIR) foams. The red arrow indicates the foam rise direction. Reproduced from [4], [5] and [10], respectively, with permission from Elsevier.

mations of cell walls. As the load increases, cell walls start to buckle elastically or collapse plastically. The elastic buckling and plastic collapse are localized failure modes, which occur first in the weakest cell walls and gradually propagate through the entire mesostructure, resulting in a plateau region with the compressive stress almost constant. Besides, the cell wall elastic buckling is the leading failure mode for low-density foams, while plastic collapse the corresponding failure mode for high-density foams [11, 12, 13, 14, 15]. Finally, upon densification the severely deformed cell walls come to contact and interact, leading to a rapid increase of the compressive stiffness.

To guide the closed-cell foam design, numerous studies have been conducted on the structure-property relationships. Among different mesostructural features, relative density is recognized as the most important in determining the compressive modulus and strength [8]. The relationships between these compressive properties and relative density have been well established. They can be expressed through power functions regardless of specific mechanisms [8]. Other features are implicitly accounted for by a set of constants of proportionality, usually identified from the experimental data. These relationships have demonstrated great success for a variety of foams (see e.g. aluminium [16, 17, 18], polyvinylchlorid (PVC) [19, 7, 9], aluminium composite [20, 21], ceramic [22] and carbon [23] foams).

In addition, many closed-cell foams exhibit apparent anisotropic properties under compression (see e.g. aluminium [24, 25, 4, 26], PVC [27, 7, 9] and polyurethane (PU) [28, 29, 30] foams). For instance, the compressive modulus and strength in the foam rise direction (see Figure 1), are noticeably higher than the transverse direction. This mechanical anisotropy has been understood to primarily originate from cell shape anisotropy (see e.g. [24, 25, 4, 28, 26, 29, 30, 27, 7, 9]), while base material anisotropy plays a secondary role [31]. These facts motivate detailed investigations on the impacts of cell shape anisotropy, arguably the second most important mesostructural feature for tailoring the compressive properties.

Compared with relative density, precisely controlling cell shape anisotropy is hardly possible in experiments, and thus micromechanical modeling is often employed. By idealizing a foam mesostructure as rectangular parallelepiped cell, Gibson and Ashby [32] pioneeringly proposed a simple semi-analytical model to predict the anisotropy of compressive properties in terms of cell shape anisotropy. It is assumed that the cell edge bending (accompanied by face tension along the direction perpendicular to the compressive loading) and cell wall plastic collapse are the dominant deformation and failure modes, respectively. Later on, Gong et al. [33], Sullivan et al. [34] and Andersons et al. [10] improved the Gibson-Ashby model by introducing Kelvin cell, which could more accurately represent a foam mesostructure¹. The idealized cell-based analytical models have been widely applied for realistic foams, showing capabilities to capture the general trends in the experimental data (see e.g.

¹These Kelvin cell-based analytical models are in principle developed for open-cell foams despite being applied for closed-cell foams in many studies.

[32, 33, 34, 35, 10, 36, 27, 9]). However, the predictive deviations vary significantly from one case to another (sometimes $> 100\%$), and are commonly regarded to arise from different uncertainties in the real foam mesostructures and experiments. Limited attention is paid to the mechanistic assumptions that has been introduced, which conflict with a few detailed experimental observations. For example, the cell wall elastic buckling, rather than plastic collapse, dominates the failure of many low-density foams (see e.g. aluminium [37], PVC [38, 13, 39, 40], PU [14, 41] and polymethacrylimide (PMI) [12, 42] foams). *This asks for a deeper understanding of the underlying mechanisms as well as the impacts of mesostructural features.*

To investigate the foam deformation behavior in detail, finite element (FE) micromechanical modeling has been extensively performed. First, numerical models based on the idealized cell structures are developed (see e.g. rectangular [43], Kelvin [44, 45, 46, 47, 48, 15, 49, 50] and Weaire–Phelan [48, 49] cells), allowing for a systematic study of different mesostructural features and mechanisms. For example, Simone and Gibson [44] reported that both the compressive modulus and strength did not vary significantly against the cell edge/face material partitioning, suggesting that closed-cell foams deformed primarily by the cell wall stretching. Grenestedt and Bassinet [45] found that the cell wall thickness stochastics only weakly affected the compressive modulus, likely because the cell wall membrane deformation dominated the initial elastic region. Chen et al. [48] and Duan et al. [15] confirmed that the failure of low-density foams was triggered by the cell wall elastic buckling, in alignment with experimental observations [11, 12, 13, 14, 15]. To the authors’ best knowledge, the idealized cell-based numerical models are rarely employed to investigate the impacts of cell shape anisotropy (see one study in [47], where no detailed mechanistic discussion is given).

Along with the advancement of computer tomography (CT) techniques, CT-based numerical models have also been developed (see e.g. [51, 52, 53, 54, 55, 56, 57, 58, 59]). These models provide a high-fidelity tool to study the underlying mechanisms. For instance, Sun et al. [55] showed that the minimal ratio of the cell wall thickness to cell size determined the weakest region, where the first collapse (or crush) band formed under compression. Similar results were reported by Chen et al. [56] and Ghazi et al. [58], that the larger and thinner cell walls tended to buckle earlier, followed by plastic deformation, eventually developing into the collapse bands. Most CT-based models are discretized by turning the voxels into cubic elements (see e.g. [54, 55]) or tetrahedral elements after geometric reconstruction (see e.g. [52, 53, 56]), leading to high computational costs. Therefore, CT-based models discretized by shell elements have been proposed, exhibiting excellent computational efficiency while preserving accuracy [51, 59]. Nevertheless, due to the inflexibility of manipulating the geometrical configurations, CT-based models are rarely used to systematically investigate the impacts of mesostructural features.

To fairly approximate the real foam mesostructures and meanwhile preserve the flexibility of manipulation, tessellation-based numerical models have received the most attention. Using Voronoi tessellation techniques, cell shape irregularity and randomness can be included. Song et al. [60] compared the results obtained using the tessellation-based and idealized cell-based models, showing that the compressive strength decreased along with cell shape irregularity. Further studies by Shi et al. [61] and Vengatachalam et al. [62] revealed that this strength reduction was attributed to the emergence of weak regions induced by cell shape irregularity. In contrast, the compressive modulus receives limited influence from cell shape irregularity, indicating that the cell wall membrane deformation dominates the initial elastic region [61] (see also [45]). Roberts and Garboczi [63], and Köll and Hallström [64] studied the impacts of cell edge/face material partitioning on the compressive modulus, and observed substantial mismatch between the numerical data and Gibson–Ashby model predictions. It is pointed out that the cell wall membrane contribution is non-negligible.

More recently, Laguerre tessellation-based models have been developed, which enable

to incorporate the cell size stochastics. Chen et al. [65, 66] showed that both the compressive modulus and strength decreased as the cell size and cell wall thickness stochastics increased, which again could be explained using the weakest link principle (see also [61, 62]). Compared with the compressive modulus, the strength is more sensitive to these mesostructural stochastics. By elongating the original tessellation structures, the anisotropic foam mesostructural models, can be generated (see e.g. [67, 68, 29, 69, 70, 71, 9, 72]). Gahlen and Stommel et al. [73, 74] further improved them to prescribe cell shape anisotropy stochastics. With the cell shape anisotropy control, the Laguerre tessellation-based models have shown great success to reproduce the anisotropic compressive stress-strain curves, even in quantitative agreement with the experimental data.

Nevertheless, very few of the above numerical studies provide quantitative analysis of the cell wall deformation behavior and elaborate how cell shape anisotropy leads to mechanical anisotropy. Attempts have been made in [29, 69, 72], on PU foams where $> 80\%$ of base materials are occupied by cell edges². Through detailed analysis of the cell edge forces, it is revealed that the compressive load applied in the foam rise direction is initially carried by the cell edge axial deformation. The compressive load applied in the transverse direction is carried by both axial and bending deformations, leading to less stiff response and buckling at a lower applied stress. These findings are consistent with the experimental observations in [30] and rationalize the anisotropic compressive properties of PU foams. Yet, the obtained insights may not be representative for many foams with a high cell face fraction (likely > 0.8 , see e.g. aluminium [24, 25, 4, 26], PVC [27, 7, 9] and PMI [42, 75] foams).

To summarize, it is believed that the anisotropic compressive properties of closed-cell foams mainly originate from cell shape anisotropy. Analytical models have been proposed in the literature which relates mechanical anisotropy to cell shape anisotropy. However, the introduced mechanistic assumptions may not be valid for the foams with a high cell face fraction and low relative density. In these cases, the cell face contribution gets crucial and the cell wall elastic buckling becomes the leading failure mode. Extensive numerical studies have further suggested that the cell wall membrane deformation dominates the initial elastic region, which, nevertheless, are lacking confirmation of the cell wall deformations, especially for anisotropic foams. Recently, attempts have been made to unravel the anisotropic compressive properties through quantitative analysis of the cell wall behavior. However, these studies focus on the foams with a low cell face fraction and thus may not be representative for many other foams. *More importantly, the detailed relationships between mechanical anisotropy and cell shape anisotropy remain unclear.*

In addition, the intrinsic randomness of mesostructural features have been found to affect the compressive properties and may also impact mechanical anisotropy. *These variations are usually overlooked when attempting to untangle the anisotropic compressive properties.* Accordingly, the present paper aims at addressing the following interconnected questions:

1. What are the key deformation mechanisms governing the anisotropic compressive behavior of closed-cell foams with a high cell face fraction and low relative density?
2. How does cell shape anisotropy translate into the anisotropy of compressive properties?
3. Is this mechanical anisotropy influenced by the mesostructural stochastics?

To the end, a systematic numerical study on the anisotropic compressive behavior is conducted, which takes into account cell shape anisotropy, cell structure and the stochastic variations of different mesostructural features. Representative volume elements (RVE) of foam mesostructures are modeled³, where cell walls are described as Reissner-Mindlin shells

²These foams can be modeled in practice as open-cell foams since the cell face contribution is negligible.

³Due to the large randomness of mesostructural features, RVE should be interpreted as statistical volume element (SVE) [76]. We retain the term RVE for consistency with convention in the foam community.

[77] in a finite rotation setting [78]. A mixed stress-strain driven homogenization scheme (see e.g. [79, 80, 81]) is adopted to formulate the RVE problem such that an overall uniaxial stress state can be enforced. In addition, to quantify the cell wall deformation behavior, a strain energy partitioning indicator is proposed, followed by a buckling occurrence detector.

Rectangular parallelepiped cell structures with different shape anisotropy are first modeled. Second, Kelvin cell structures are modeled which further account for the cell wall inclination angle. Third, foam mesostructures generated using Laguerre tessellation techniques are modeled which incorporate the stochastic variations of cell size, cell wall thickness and cell shape anisotropy. Based on the numerical analyses of the two idealized cell-based models, analytical models are derived which relates the anisotropy of compressive properties to cell shape anisotropy. The mechanical anisotropy determined from the tessellation-based numerical models is compared against the present analytical model predictions, to identify the influence of mesostructural stochastics. Besides, two widely used analytical models [32, 34] are assessed, to investigate the importance of imposing appropriate mechanistic assumptions. This contribution will provide a deeper understanding on the relationships between the anisotropic compressive properties and mesostructural features.

The paper is organized as follows. In Section 2, the foam mesostructural RVE problem is formulated. In Section 3, a general quantification method for the cell wall deformation behavior is introduced. In Section 4, RVE simulation setup is elaborated. In Section 5, numerical results of the idealized cell-based models (rectangular parallelepiped and Kelvin cells) are analyzed. Based on the insights obtained, analytical models that describe the relationships between mechanical anisotropy and cell shape anisotropy are developed in Section 6. In Section 7, numerical results of the tessellation-based models are analyzed. The extracted anisotropy of compressive properties is compared against the analytical model predictions as well as experimental data, followed by discussions on the impacts of mesostructural stochastics. The main conclusions are summarized in Section 8.

Scalars, vectors, second-order tensors and forth-order tensors in this paper are denoted as e.g. a , \vec{a} , \mathbf{A} and \mathbb{A} , respectively. The length of a vector (Euclidean norm) is denoted by $\|\vec{\bullet}\|$. The transpose and inverse of a second-order tensor are denoted by $(\bullet)^T$ and $(\bullet)^{-1}$, respectively. The macroscale effective quantities are denoted by (\bullet) .

2. RVE problem description

Consider a foam mesostructural RVE (see Figure 2(a)), with its space-filling volume domain (shaded green) indicated by \mathcal{V} and base material volume domain by \mathcal{V}_r . Only a single cell structure is illustrated for simplicity. Reissner–Mindlin shell description [77] is adopted for the cell walls. The shell reference mid-surface is denoted by \mathcal{A}_r and external boundary contour by \mathcal{C}_r . The global coordinate system $\{\vec{e}_1, \vec{e}_2, \vec{e}_3\}$ is chosen such that \vec{e}_3 is parallel to the foam rise direction, and \vec{e}_1 and \vec{e}_2 the two transverse directions.

2.1. Shell kinematics and stress resultants

To capture geometrically nonlinear behavior of cell walls, a finite rotation shell formulation [78] is adopted. Let introduce a curvilinear coordinate system $\{\vec{e}_1^c, \vec{e}_2^c, \vec{e}_3^c\}$, such that the plane $\{\vec{e}_1^c, \vec{e}_2^c\}$ is tangent to the mid-surface, while \vec{e}_3^c is normal to this tangent plane. Position vectors of any material point in the initial and current configurations are given by

$$\vec{X} = \vec{X}_r + \eta \vec{D}, \quad \eta \in \mathcal{H} \quad (1a)$$

$$\vec{x} = \vec{x}_r + \eta \vec{d}, \quad \eta \in \mathcal{H} \quad (1b)$$

where \vec{X}_r and \vec{x}_r define a point on the mid-surface before and after deformation, respectively; \vec{D} denotes the director in the initial configuration, coincident with the local normal to the

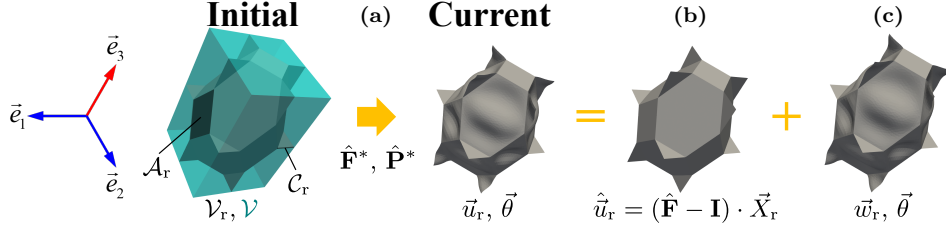


Figure 2: A foam mesostructural RVE with cell walls described as shell continuum: (a) initial to current configurations after imposing the macroscale stress $\hat{\mathbf{P}}$ and deformation gradient $\hat{\mathbf{F}}$ in a mixed manner. $(\bullet)^*$ indicates a quantity with its components partially prescribed. The space-filling volume domain including voids are indicated by the green shadows; decomposition of the mesoscale mid-surface displacement field $\tilde{\mathbf{u}}_r$ into the (b) trend field $\hat{\mathbf{u}}_r$ and (c) fluctuation field $\tilde{\mathbf{w}}_r$. The rotation angle field $\vec{\theta}$ is not visible.

undeformed mid-surface, i.e. $\vec{D} = \vec{e}_3^c$; \vec{d} denotes the director in the current configuration, which is, in general, non-coincident with the local normal to the deformed mid-surface, thus enabling to describe the change of shell thickness and transverse shear effects; η is the through-thickness coordinate, belonging to the thickness domain $\mathcal{H} = [-\frac{t}{2}, \frac{t}{2}]$, with t the thickness which can vary from one location of \vec{X}_r to another.

Following Reissner–Mindlin shell theory such that any thickness change during the deformation can be disregarded, \vec{d} is related to \vec{D} through a rotation tensor \mathbf{R} as

$$\vec{d} = \mathbf{R} \cdot \vec{D}. \quad (2)$$

Here, \mathbf{R} may be expressed in terms of the Euler rotation angle vector $\vec{\theta}$, according to the well-known Euler–Rodrigues formula

$$\mathbf{R}(\vec{\theta}) = \mathbf{I} + h_1(\theta)\boldsymbol{\Theta} + h_2(\theta)\boldsymbol{\Theta} \cdot \boldsymbol{\Theta}, \quad (3)$$

where \mathbf{I} denotes the second-order identity tensor, $\theta = \|\vec{\theta}\|$ the true rotation angle and $\boldsymbol{\Theta} = \text{skew}(\vec{\theta})$ the skew-symmetric tensor whose axial vector is $\vec{\theta}$; h_1 and h_2 are two trigonometric functions in terms of θ

$$h_1(\theta) = \frac{\sin \theta}{\theta}, \quad h_2(\theta) = \frac{1}{2} \left(\frac{\sin(\theta/2)}{\theta/2} \right)^2. \quad (4)$$

Subtracting eq. (1a) from eq. (1b) gives the displacement field as

$$\vec{u} = \vec{u}_r + (\mathbf{R} - \mathbf{I}) \cdot \eta \vec{D}, \quad (5)$$

implying that the finite rotation shell kinematics can be fully parametrized using \vec{u}_r and $\vec{\theta}$.

The deformation gradient tensor follows from eq. (1) as (see [82, 83] for detailed derivations)

$$\mathbf{F} = (\vec{\nabla}_0 \vec{x})^T = \left(\frac{\partial \vec{x}_r}{\partial \vec{X}_r} \right)^T + \eta \left(\frac{\partial \vec{d}}{\partial \vec{X}_r} \right)^T + \vec{d} \otimes \vec{D}, \quad (6)$$

where $\vec{\nabla}_0 = \partial(\bullet)/\partial \vec{X}_r + \partial(\bullet)/\partial(\eta \vec{D})$ denotes the gradient operator with respect to \vec{X} . Substituting eq. (2) into eq. (6) yields

$$\mathbf{F} = \mathbf{L} + \eta \mathbf{K}, \quad (7)$$

with

$$\mathbf{L} = (\tilde{\tilde{\nabla}}_0 \otimes \vec{x}_r)^T + \mathbf{R} \cdot \vec{D} \otimes \vec{D}, \quad (8a)$$

$$\mathbf{K} = \boldsymbol{\Gamma} \cdot \left(\tilde{\tilde{\nabla}}_0 \otimes (\vec{\theta} \times \vec{D}) \right)^T, \quad (8b)$$

where $\tilde{\tilde{\nabla}}_0 = \partial(\bullet)/\partial \vec{X}_r$ denotes the gradient operator with respect to \vec{X}_r ; the tensor $\boldsymbol{\Gamma}$ introduced in eq. (8b) is given by

$$\boldsymbol{\Gamma}(\vec{\theta}) = \mathbf{I} + h_2(\theta)\boldsymbol{\Theta} + h_3(\theta)\boldsymbol{\Theta} \cdot \boldsymbol{\Theta}, \quad (9)$$

with the trigonometric function

$$h_3(\theta) = \frac{1 - h_1(\theta)}{\theta^2}. \quad (10)$$

For the convenience of constitutive model formulation, a back-rotated configuration is introduced by eliminating \mathbf{R} . The back-rotated counterpart of \mathbf{F} is given by

$$\mathbf{F}^c = \mathbf{R}^T \cdot \mathbf{F} = \mathbf{I} + \mathbf{H}^c + \eta \mathbf{K}^c, \quad (11)$$

where $\mathbf{H}^c = \mathbf{R}^T \cdot \mathbf{L} - \mathbf{I}$ and $\mathbf{K}^c = \mathbf{R}^T \cdot \mathbf{K}$ represent the cross-sectional generalized strain and bending curvature, respectively

$$\mathbf{H}^c = \mathbf{R}^T \cdot (\tilde{\tilde{\nabla}}_0 \otimes \vec{x}_r)^T - \tilde{\tilde{\mathbf{I}}}, \quad (12a)$$

$$\mathbf{K}^c = \boldsymbol{\Gamma}^T \cdot \left(\tilde{\tilde{\nabla}}_0 \otimes (\vec{\theta} \times \vec{D}) \right)^T, \quad (12b)$$

with $\tilde{\tilde{\mathbf{I}}} = (\tilde{\tilde{\nabla}}_0 \otimes \vec{X}_r)^T = \mathbf{I} - \vec{D} \otimes \vec{D}$. Here, equation (8) has been substituted and the property $\boldsymbol{\Gamma}^T = \mathbf{R}^T \cdot \boldsymbol{\Gamma}$ has been applied. The membrane strain tensor $\tilde{\tilde{\mathbf{H}}}^c$ and transverse shear strain vector \vec{G}^c can be identified from \mathbf{H}^c as

$$\tilde{\tilde{\mathbf{H}}}^c = \tilde{\tilde{\mathbf{I}}} \cdot \mathbf{H}^c, \quad (13a)$$

$$\vec{G}^c = \vec{D} \cdot \mathbf{H}^c. \quad (13b)$$

The shell kinetics is typically described by the through-thickness resultant quantities. Denoting the first Piola–Kirchhoff stress tensor by \mathbf{P} and thus its back-rotated counterpart $\mathbf{P}^c = \mathbf{R}^T \cdot \mathbf{P}$, the resultants conjugate to $\tilde{\tilde{\mathbf{H}}}^c$, \vec{G}^c and \mathbf{K}^c are defined as

$$\tilde{\tilde{\mathbf{N}}}^c = \tilde{\tilde{\mathbf{I}}} \cdot \int_{\mathcal{H}} \mathbf{P}^c d\eta, \quad (14a)$$

$$\vec{V}^c = \vec{D} \cdot \int_{\mathcal{H}} \mathbf{P}^c d\eta, \quad (14b)$$

$$\mathbf{M}^c = \int_{\mathcal{H}} \eta \mathbf{P}^c d\eta, \quad (14c)$$

representing the membrane stress resultant tensor, transverse shear stress resultant vector and bending moment tensor, respectively. The constitutive relations between $\{\tilde{\tilde{\mathbf{N}}}^c, \vec{V}^c, \mathbf{M}^c\}$ and $\{\tilde{\tilde{\mathbf{H}}}^c, \vec{G}^c, \mathbf{K}^c\}$ will be specified in [Section 4](#).

Similarly, the resultants conjugate to \mathbf{L} and \mathbf{K} are defined as

$$\mathbf{N} = \int_{\mathcal{H}} \mathbf{P} d\eta, \quad (15a)$$

$$\mathbf{M} = \int_{\mathcal{H}} \eta \mathbf{P} \, d\eta. \quad (15b)$$

Following the Reissner–Mindlin theory such that a plane stress state can be assumed in the thickness direction, and making use of the principle $\int_{\mathcal{H}} \delta \mathbf{F}^T : \mathbf{P} \, d\eta = \int_{\mathcal{H}} (\delta \mathbf{F}^c)^T : \mathbf{P}^c \, d\eta$, \mathbf{N} and \mathbf{M} can be expressed in terms of $\tilde{\mathbf{N}}^c$, \vec{V}^c and \mathbf{M}^c as

$$\mathbf{N} = \mathbf{R} \cdot (\tilde{\mathbf{N}}^c + \vec{D} \otimes \vec{V}^c), \quad (16a)$$

$$\mathbf{M} = \mathbf{R} \cdot \mathbf{M}^c. \quad (16b)$$

2.2. Weak form of the balance equations

The mid-surface displacement \vec{u}_r and rotation angle $\vec{\theta}$ are commonly adopted as the primary field variables to be solved for a finite rotation shell problem. In absence of body force, the weak form can be stated as: find $\{\vec{u}_r, \vec{\theta}\}$ such that for all admissible variations $\{\delta \vec{u}_r, \delta \vec{\theta}\}$, the balance holds between the internal and external virtual works (see also [78]):

$$\int_{\mathcal{A}_r} \delta \mathbf{L}^T(\vec{u}_r, \vec{\theta}) : \mathbf{N} \, dA + \int_{\mathcal{A}_r} \delta \mathbf{K}^T(\vec{\theta}) : \mathbf{M} \, dA = \int_{\mathcal{C}_r} \delta \vec{u}_r \cdot \vec{n} \, dC + \int_{\mathcal{C}_r} \delta \vec{\theta} \cdot (\mathbf{F}^T(\vec{\theta}) \cdot \vec{m}) \, dC, \quad \forall \{\delta \vec{u}_r, \delta \vec{\theta}\}, \quad (17)$$

with the traction resultant and bending moment on the external boundary \mathcal{C}_r given by

$$\vec{n} = \mathbf{N} \cdot \vec{N}_r, \quad \vec{m} = \mathbf{M} \cdot \vec{N}_r \quad \text{on } \mathcal{C}_r. \quad (18)$$

Here \vec{N}_r is the outward normal to \mathcal{C}_r . The boundary conditions required to complete the problem (17) will be determined through downscaling. The standard strain driven formulation will be introduced first, and then extended to a mixed stress-strain driven formulation.

2.3. Standard strain driven formulation

Following the classical homogenization (see e.g. [84, 85]), applying the macroscale effective deformation gradient tensor $\hat{\mathbf{F}}$ to the foam mesostructural RVE (see Figure 2(a)) yields the mesoscale relative position vector field, over the space-filling volume \mathcal{V}

$$\Delta \vec{x} = \hat{\mathbf{F}} \cdot \Delta \vec{X} + \Delta \vec{w}, \quad \vec{X} \in \mathcal{V} \quad (19)$$

with $\Delta \vec{X} = \vec{X} - \vec{X}_o$, $\Delta \vec{x} = \vec{x} - \vec{x}_o$ and $\Delta \vec{w} = \vec{w} - \vec{w}_o$, where \vec{X}_o denotes the initial position vector of a reference origin point; the current position vector of this point is denoted by \vec{x}_o ; \vec{w} reflects the fluctuations induced by heterogeneities.

The classical downscaling requires that the volume average of the mesoscale deformation gradient \mathbf{F} is equated to the macroscale deformation gradient $\hat{\mathbf{F}}$ (see also [84, 85]):

$$\hat{\mathbf{F}} = \frac{1}{V} \int_{\mathcal{V}} \mathbf{F} \, dV, \quad (20)$$

with V the RVE space-filling volume (see Figure 2(a)). Substituting eqs. (6) and (19) into eq. (20), followed by applying divergence theorem, gives the constraint in terms of the fluctuations $\Delta \vec{w}$

$$\int_{\partial \mathcal{V} / \partial \mathcal{V}_r} \Delta \vec{w} \otimes \vec{N} \, d\partial V + \int_{\partial \mathcal{V}_r} \Delta \vec{w} \otimes \vec{N} \, d\partial V = \mathbf{0}. \quad (21)$$

where the total external surface domain $\partial \mathcal{V}$ has been split into the void $\partial \mathcal{V} / \partial \mathcal{V}_r$ and base material $\partial \mathcal{V}_r$ parts. Note, that $\Delta \vec{w}$ is not available on $\partial \mathcal{V} / \partial \mathcal{V}_r$ as the void part is not involved

in the RVE problem. Therefore, the following choice is made to satisfy constraint (21)

$$\int_{\partial\mathcal{V}/\partial\mathcal{V}_r} \Delta\vec{w} \otimes \vec{N} d\partial V = \mathbf{0}, \quad (22a)$$

$$\int_{\partial\mathcal{V}_r} \Delta\vec{w} \otimes \vec{N} d\partial V = \mathbf{0}. \quad (22b)$$

The first constraint can be fulfilled by appropriate choice of $\Delta\vec{w}$ on $\partial\mathcal{V}/\partial\mathcal{V}_r$, which in practice does not affect the RVE solution.

Constraint (22b) is next elaborated. For the convenience of derivations, let choose the reference origin point \vec{X}_o to be located within the mid-surface of cell walls. Moreover, the fluctuation at \vec{X}_o will be constrained, i.e. $\vec{w}_o = \vec{0}$, to eliminate the rigid-body translation.

Consistent with the shell kinematics (1), \vec{w} at any material point can be expressed as

$$\vec{w} = \vec{w}_r + \left(\mathbf{R}(\vec{\theta}) - \hat{\mathbf{R}} \right) \cdot \eta \vec{D}, \quad \eta \in \mathcal{H} \quad (23)$$

where \vec{w}_r collects the mid-surface displacement fluctuations, while the other term collects the director fluctuations; $\hat{\mathbf{R}}$ is the rotation part of $\hat{\mathbf{F}}$. Substituting eq. (23) into eq. (22b) leads to the constraint in terms of \vec{w}_r and $\vec{\theta}$:

$$\int_{C_r} \int_{\mathcal{H}} \left(\vec{w}_r + \left(\mathbf{R}(\vec{\theta}) - \hat{\mathbf{R}} \right) \cdot \eta \vec{D} \right) \otimes \vec{N}_r d\eta dC = \mathbf{0}. \quad (24)$$

Further taking into account the thickness domain $\mathcal{H} = [-\frac{t}{2}, \frac{t}{2}]$, constraint (24) can be simplified into

$$\int_{C_r} t \vec{w}_r \otimes \vec{N}_r dC = \mathbf{0}, \quad (25)$$

implying that the constraints on $\vec{\theta}$ are in principle not compulsory for a symmetric shell formulation.

The standard strain driven homogenization scheme assumes that $\hat{\mathbf{F}}$ is fully known and thus the mesoscale mid-surface displacement fluctuation field \vec{w}_r can be replaced by

$$\vec{w}_r = \vec{u}_r - (\hat{\mathbf{F}} - \mathbf{I}) \cdot \vec{X}_r. \quad (26)$$

Substituting eq. (26) into eq. (25) yields minimal kinematic boundary conditions in terms of the mesoscale mid-surface displacements \vec{u}_r

$$\int_{C_r} t \vec{u}_r \otimes \vec{N}_r dC = (\hat{\mathbf{F}} - \mathbf{I}) \cdot \int_{C_r} t \vec{X}_r \otimes \vec{N}_r dC. \quad (27)$$

The other common choice to fulfil constraint (25) is fully prescribed boundary conditions, which can be obtained by enforcing $\vec{w}_r = \vec{0}$ on the external boundary C_r

$$\vec{u}_r = (\hat{\mathbf{F}} - \mathbf{I}) \cdot \vec{X}_r \quad \text{on } C_r \quad (28)$$

For an RVE with geometrical periodicity and thus anti-periodicity on the external boundary normals, i.e. $\vec{N}_r^- = -\vec{N}_r^+$, periodic boundary conditions is often adopted

$$\vec{u}_r^- - \vec{u}_r^+ = (\hat{\mathbf{F}} - \mathbf{I}) \cdot (\vec{X}_r^- - \vec{X}_r^+) \quad \text{on } C_r \quad (29)$$

Here the superscripts “-/+” denote the opposite boundary pair. Notice that many foam mesostructural RVE studies (see e.g. [48, 73, 72]) introduce extra conditions $\vec{\theta}^- = \vec{\theta}^+$,

along with conditions (29). This combination intuitively follows from the periodic boundary conditions for the solid continuum problem and directly fulfils constraint (24).

Choosing one of the conditions (27), (28) and (29) completes the RVE problem (17). After solving the RVE problem, the macroscale effective stress $\hat{\mathbf{P}}$ can be derived using the Hill-Mandel condition [86], as the volume average of the mesoscale stress \mathbf{P} (see also [84, 85])

$$\hat{\mathbf{P}} = \frac{1}{V} \int_{\mathcal{V}} \mathbf{P} \, dV. \quad (30)$$

Accounting for $\mathbf{P} = \mathbf{0}$ in the void part $\mathcal{V}/\mathcal{V}_r$, substituting eq. (15a) into eq. (30) gives $\hat{\mathbf{P}}$ in terms of the mesoscale resultants \mathbf{N} :

$$\hat{\mathbf{P}} = \frac{1}{V} \int_{\mathcal{A}_r} \mathbf{N} \, dA = \frac{1}{V} \int_{\mathcal{C}_r} \vec{n} \otimes \vec{X}_r \, dC. \quad (31)$$

Here, divergence theorem has been applied to obtain the second equality. Clearly, the mesoscale resultant \mathbf{M} (see eq. (15b)) does not contribute to $\hat{\mathbf{P}}$.

2.4. Mixed stress-strain driven formulation

The RVE response under a specific stress state, e.g. overall stress free or uniaxial stress (to be considered in this study) state, is of interest in some cases. This is, however, not straightforward to achieve with the strain driven formulation. To address this challenge, several mixed stress-strain driven formulations for the solid continuum problem that enable to prescribe $\hat{\mathbf{P}}$ or $(\hat{\mathbf{F}}, \hat{\mathbf{P}})$ in a mixed manner, have been proposed in the literature (see e.g. [79, 80, 81]). Following the same spirit, the early introduced strain driven formulation for the shell problem is subsequently extended to a mixed stress-strain driven formulation.

As sketched in Figure 2 (see also eq. (26)), the mesoscale mid-surface displacement field \vec{u}_r consists of two contributions:

$$\vec{u}_r = \hat{\vec{u}}_r + \vec{w}_r = (\hat{\mathbf{F}} - \mathbf{I}) \cdot \vec{X}_r + \vec{w}_r, \quad (32)$$

where the first term represents a linear, trend field induced by $\hat{\mathbf{F}}$ while the second term \vec{w}_r the fluctuation field. Considering $\hat{\mathbf{F}}$, \vec{w}_r and $\vec{\theta}$ as the primary field variables instead, substituting eq. (32) into eq. (17) allows to reformulate the RVE problem as:

$$\begin{aligned} & \int_{\mathcal{A}_r} \delta \mathbf{L}^T(\hat{\mathbf{F}}, \vec{w}_r, \vec{\theta}) : \mathbf{N} \, dA + \int_{\mathcal{A}_r} \delta \mathbf{K}^T(\vec{\theta}) : \mathbf{M} \, dA \\ & = V \delta \hat{\mathbf{F}}^T : \hat{\mathbf{P}} + \int_{\mathcal{C}_r} \delta \vec{w}_r \cdot \vec{n} \, dC + \int_{\mathcal{C}_r} \delta \vec{\theta} \cdot (\boldsymbol{\Gamma}^T(\vec{\theta}) \cdot \vec{m}) \, dC, \quad \forall \{\delta \hat{\mathbf{F}}, \delta \vec{w}_r, \delta \vec{\theta}\}. \end{aligned} \quad (33)$$

Here, equation (31) has been applied to the right-hand side as such $\hat{\mathbf{P}}$ appears like an “external force”, which can be prescribed.

Accordingly, the RVE boundary conditions (27), (28) and (29) derived from the strain driven homogenization are reformulated in terms of \vec{w}_r . Constraint (25) can be directly adopted as minimal kinematic boundary conditions. Fully prescribed boundary conditions and periodic boundary conditions become $\vec{w}_r = \vec{0}$ and $\vec{w}_r^- = \vec{w}_r^+$, respectively.

3. Quantification method of the cell wall behavior

To directly identify the deformation mechanisms, a quantification method for the cell wall deformation behavior is developed. As discussed in Section 1, cell wall stretching and bending are the two most commonly observed deformation modes. Accordingly, one choice is

to measure the partition of strain energy in cell walls into membrane and bending modes (see also e.g. [87, 88]). A cell wall-wise (marked by the subscript “w”) strain energy partitioning indicator \mathcal{I}_w is defined through:

$$\mathcal{I}_w = \frac{W_w^b - W_w^m}{W_w^b + W_w^m}, \quad (34)$$

with W_w^m and W_w^b being the membrane and bending energy, respectively. $\mathcal{I}_w = -1$ indicates a pure membrane deformation mode while $\mathcal{I}_w = 1$ a pure bending mode. Making use of the shell kinetic quantities (see eqs. (12)-(14)), W_w^m and W_w^b can be evaluated as

$$W_w^m = \int_{\mathcal{A}_w} \left(\int (\tilde{\mathbf{N}}^c)^T : d\tilde{\mathbf{H}}^c \right) dA, \quad (35a)$$

$$W_w^b = \int_{\mathcal{A}_w} \left(\int (\mathbf{M}^c)^T : d\mathbf{K}^c \right) dA, \quad (35b)$$

with \mathcal{A}_w being the mid-surface of a probed cell wall. Notice that the proposed indicator (34) is applicable to an arbitrary constitutive model choice, in contrast to those in the literature where small strain and isotropic elasticity are assumed (see e.g. [87, 88]).

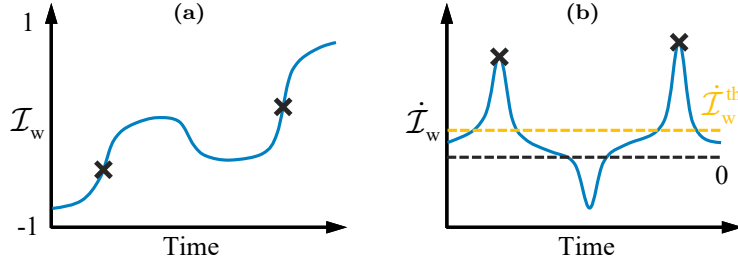


Figure 3: Sketches of the strain energy partitioning (a) indicator \mathcal{I}_w and (b) indicator rate $\dot{\mathcal{I}}_w$ versus time, for a probed cell wall. The occurrence of buckling is indicated by the black crosses.

For low-density foams, the cell wall elastic buckling is the main failure mode (see Section 1). Therefore, the occurrence of buckling is also tracked. As buckling is often accompanied by a sharp transition from the membrane to bending mode, a sudden increase on the indicator profile \mathcal{I}_w is expected, as sketched in Figure 3(a). This sudden increase may be characterized as a positive peak on the rate profile $\dot{\mathcal{I}}_w$, as sketched in Figure 3(b). A cell wall-wise buckling occurrence detector \mathcal{D}_w is proposed, which is defined in a time-wise way:

$$\mathcal{D}_w^n = \begin{cases} 1 & \text{if } \dot{\mathcal{I}}_w^n > \max\{\dot{\mathcal{I}}_w^{n-1}, \dot{\mathcal{I}}_w^{n+1}\} \text{ and } \dot{\mathcal{I}}_w^n > 0 \text{ and } \dot{\mathcal{I}}_w^n > \dot{\mathcal{I}}_w^{\text{th}}, \\ 0 & \text{else} \end{cases}, \quad (36)$$

where n indicates the probed time step, and a threshold $\dot{\mathcal{I}}_w^{\text{th}}$ is introduced to extract remarkable peaks only. The threshold value is proposed as the time average of $\dot{\mathcal{I}}_w$. A cell wall will be considered “buckled” as long as $\mathcal{D}_w = 1$ appears once in the time range of interest.

4. RVE numerical simulation setup

4.1. Geometrical model configurations

To systematically investigate the influence of different foam mesostructural features, RVE models with different levels of complexity are considered. Since a high cell face fraction is focused on, constant thickness is assumed for each cell wall (see also e.g. [65, 62, 9]). For each cell (marked by the subscript “v”), the shape of which is (approximately) transversely

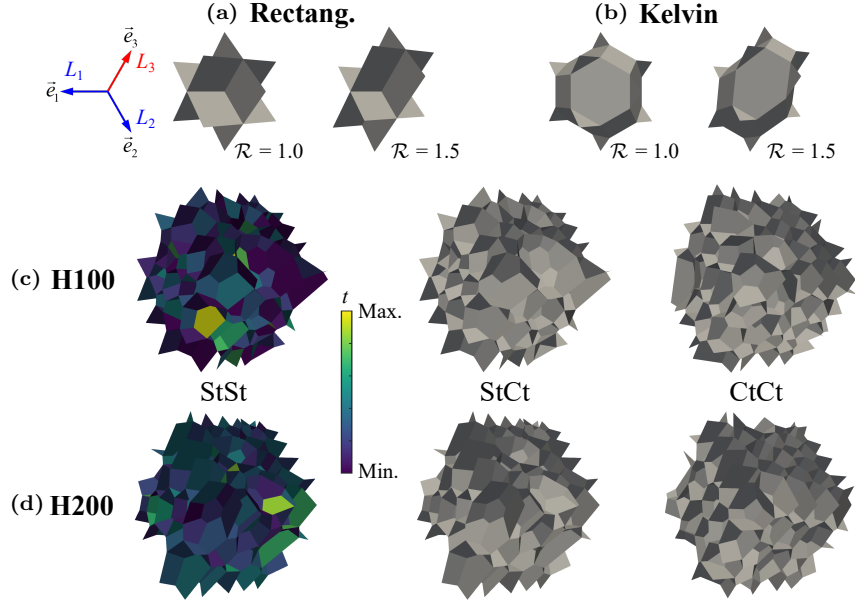


Figure 4: Geometrical model configurations of different foam mesostructural RVE: (a-b) idealized cell-based models for two shape anisotropy. All cell walls are assigned with a constant thickness; (c-d) tessellation-based models. “StSt” accounts for the stochastic variations of both cell size and cell wall thickness. “StCt” accounts for the cell size stochastics while assigning a constant thickness to all cell walls. “CtCt” assigns a constant equivalent diameter to all cells and a constant thickness to all cell walls.

isotropic, shape anisotropy is defined as $\mathcal{R}_v = (\mathcal{R}_{v,31}\mathcal{R}_{v,32})^{\frac{1}{2}}$, where the two ratios are given by $\mathcal{R}_{v,31} = l_{v,3}/l_{v,1}$ and $\mathcal{R}_{v,32} = l_{v,3}/l_{v,2}$. Here, $l_{v,i}$ denotes the cell dimension in the global direction \vec{e}_i . Besides, an equivalent diameter $d_v = (\frac{6}{\pi}V_v)^{\frac{1}{3}}$ is introduced, with V_v being the cell volume. The overall cell shape anisotropy for an RVE model consisting of multiple cells is evaluated as $\mathcal{R} = \frac{1}{N_v} \sum \mathcal{R}_v$, where N_v denotes the total number of cells (see also e.g. [6, 7, 89]). Finally, the overall relative density is evaluated as $\rho/\rho_r = V_r/V$, where ρ and ρ_r represent the RVE and base material mass densities, respectively; $V = \sum V_v = L_1L_2L_3$ the total volume of cells (or RVE space-filling volume), with L_i the RVE dimension in the global direction \vec{e}_i ; $V_r = \sum tA_w$ the total volume of cell walls, i.e. base material volume, t the cell wall thickness and A_w the cell wall mid-surface area.

The idealized cell-based models are first introduced, including rectangular parallelepiped and Kelvin cells, which have been widely employed in the literature (see e.g. [43, 47, 50]). The use of rectangular parallelepiped cells allows for investigating the impacts purely by cell shape anisotropy, while Kelvin cells further take the cell wall inclination angle into account and better approximate the real foam mesostructures. Geometrical model configurations for the two shape anisotropy, $\mathcal{R} = 1$ and $\mathcal{R} = 1.5$, are shown in Figures 4(a) and (b) as examples, with the geometrical parameters adopted for $\mathcal{R} = 1$ listed in Table 1.

By assuming periodicity, each RVE model represents a perfectly repeatable, infinite foam mesostructure. Model configurations with \mathcal{R} from 1 to 2 are considered. L_i is scaled according to the prescribed \mathcal{R} , with V and t preserved, i.e. $L_1 = L_2 = V^{\frac{1}{3}}\mathcal{R}^{-\frac{1}{3}}$ and $L_3 = V^{\frac{1}{3}}\mathcal{R}^{\frac{2}{3}}$. Note, that ρ/ρ_r would slightly increase as \mathcal{R} increases. For rectangular parallelepiped cells, ρ/ρ_r varies from 0.0750 to 0.0788 while for Kelvin cells, from 0.0837 to 0.0906. The resulting ρ/ρ_r are indeed representative for the low-density foams (see e.g. [37, 40, 42]).

Next, tessellation-based models are introduced which incorporate the stochastic variations of cell size, cell wall thickness and cell shape anisotropy observed in real foam

Table 1: Geometrical parameters of the reference idealized cell-based models ($\mathcal{R} = 1$) in Figures 4(a) and (b).

Parameter	Symbol	Rectang.	Kelvin
RVE dimension 1	L_1	0.4 [mm]	0.4 [mm]
RVE dimension 2	L_2	0.4 [mm]	0.4 [mm]
RVE dimension 3	L_3	0.4 [mm]	0.4 [mm]
Cell wall thickness	t	0.01 [mm]	0.01 [mm]
Relative density	ρ/ρ_r	0.0750 [-]	0.0837 [-]

mesostructures. Diab Divinycell foam H100 and H200 are considered, given their representativeness as low-density foams and availability of mesostructural characterization data in the literature (see e.g. [7, 5, 89]). The corresponding RVE geometrical model configurations are generated using Laguerre tessellation techniques, supported in the open-source package Neper [90], in accordance to the detailed experimental measurements [5].

For each tessellation-based RVE model, the overall cell shape anisotropy \mathcal{R} is prescribed. The resulting shape anisotropy \mathcal{R}_v of individual cells approximately follows a normal distribution (see Figures A.21(a) and (b)), associated with the cell shape irregularity. The cell equivalent diameters d_v are assigned using a log-normal distribution [5], with the mean μ_d and standard deviation σ_d . The cell wall thickness t is assigned using a gamma distribution [5], with the mean μ_t and standard deviation σ_t . The adopted geometrical parameters are listed in Table 2, with the generated model set “StSt” shown in Figures 4(c) and (d). It has been validated that the numerically realized distributions of different mesostructural features agree well with the prescribed distributions (see Figure A.21). More details can be found in Appendix A. The resulting ρ/ρ_r for “StSt” H100 and H200 are 0.0806 and 0.1480, respectively, which are slightly higher than the nominal values (see Table 2). Nevertheless, such differences are within the variation of ρ/ρ_r in practice, $+15/-10\%$ [91].

To investigate the influence of different mesostructural stochastics, two extra model sets “StCt” and “CtCt” are introduced (see Figures 4(c) and (d)), with the cell shape anisotropy stochastics close to “StSt”. “StCt” is obtained by prescribing a constant t on “StSt”, i.e. $\sigma_t = 0$ [mm]. The resulting ρ/ρ_r for “StCt” are nearly the same as “StSt”. “CtCt” is obtained by further enforcing a constant d_v on “StCt”, i.e. $\sigma_d = 0$ [mm]. Notice that the resulting ρ/ρ_r for “CtCt” H100 and H200 are 0.0922 and 0.1668, apparently higher than the nominal values (see Table 2). This implies the importance of incorporating the cell size stochastics in order to fairly approximate realistic foams.

Table 2: Geometrical parameters of the tessellation-based model set “StSt” in Figures 4(c) and (d).

Parameter	Symbol	H100	H200
RVE dimension 1	L_1	1.50 [mm]	1.45 [mm]
RVE dimension 2	L_2	1.50 [mm]	1.45 [mm]
RVE dimension 3	L_3	1.50 [mm]	1.45 [mm]
Cell shape anisotropy	\mathcal{R}	1.2 [-]	1.4 [-]
Cell equivalent diameter	(μ_d, σ_d)	(0.35, 0.10) [mm]	(0.34, 0.09) [mm]
Cell wall thickness	(μ_t, σ_t)	(0.0115, 0.0059) [mm]	(0.0200, 0.0067) [mm]
Nominal relative density	ρ/ρ_r	0.0714 [-]	0.1429 [-]

Each RVE model is discretized in the open-source mesh generator Gmsh [92], by triangular shell elements with the mid-surface displacement fluctuation \vec{w}_r and rotation $\vec{\theta}$ as degrees of freedom (DOF). To avoid shear-locking, second-order Lagrange interpolation is adopted

for \vec{w}_r while Crouzeix-Raviart interpolation for $\vec{\theta}$, as suggested in [78]. For the idealized cell-based models, a fine mesh with averaged element size ~ 0.01 [mm] is used to resolve the local deformation pattern in sufficient detail. For the tessellation-based models, a relatively large element size ~ 0.03 [mm] is chosen to balance the computational accuracy and cost. A mesh sensitivity check has been performed for each tessellation-based model, and confirmed that the cell wall-wise and macroscale effective responses are both converged for the adopted discretization. Besides, it has been confirmed that the chosen RVE dimensions (see Table 2) are sufficiently large (with ~ 120 cells) to deliver the converged effective compressive properties, even when different random realizations are considered. More details can be found in Appendix B.

4.2. Material model

This study focuses on the anisotropy of compressive modulus and strength for low-density foams, where the failure is mainly triggered by the cell wall elastic buckling (see Section 1). Therefore, plasticity is disregarded here and a finite-strain isotropic elasticity is used to describe the base material behavior. The bulk elasticity follows the linear relation $\mathbf{S} = \mathbb{C} : \mathbf{E}$, where $\mathbf{S} = \mathbf{F}^{-1} \cdot \mathbf{P}$ denotes the second Piola-Kirchhoff stress tensor, $\mathbf{E} = \frac{1}{2}(\mathbf{F}^T \cdot \mathbf{F} - \mathbf{I})$ the Green-Lagrange strain tensor, and \mathbb{C} the forth-order elasticity tensor fully determined by Young's modulus E and Poisson's ratio ν . Substituting the bulk elasticity into eqs. (12)-(14), followed by neglecting the higher-order terms, leads to the constitutive relations consistent with the finite rotation shell formulation:

$$\tilde{\mathbf{N}}^c = \tilde{\mathbf{L}}^c \cdot \mathbb{D}^m : \frac{1}{2} ((\tilde{\mathbf{L}}^c)^T \cdot \tilde{\mathbf{L}}^c - \tilde{\mathbf{I}}), \quad (37a)$$

$$\vec{V}^c = \mathbf{D}^t \cdot \vec{G}^c, \quad (37b)$$

$$\mathbf{M}^c = \tilde{\mathbf{L}}^c \cdot \mathbb{D}^b : \frac{1}{2} ((\tilde{\mathbf{L}}^c)^T \cdot \mathbf{K}^c + (\mathbf{K}^c)^T \cdot \tilde{\mathbf{L}}^c), \quad (37c)$$

with $\tilde{\mathbf{L}}^c = \tilde{\mathbf{I}} + \tilde{\mathbf{H}}^c$. Here, $\mathbb{D}^m = t\mathbb{C}^{ps}$, $\mathbf{D}^t = \frac{\kappa t E}{2(1+\nu)} \tilde{\mathbf{I}}$ and $\mathbb{D}^b = \frac{t^3}{12} \mathbb{C}^{ps}$ represent the generalized stiffness tensors for the membrane, transverse shear and bending modes, respectively; \mathbb{C}^{ps} denotes a degraded \mathbb{C} by assuming a plane stress state in the thickness direction \vec{e}_3^c ; $\kappa = \frac{5}{6}$ is the shear correction factor. Besides, a fictitious stiffness $\varepsilon t E$ is added to stabilize the drilling rotation and the factor ε is taken to be 0.02. It has been confirmed that the resulting drilling strain energy is sufficiently small.

The material model described above is implemented using the open-source code generator MFront [93]. In consistency with Divinycell foams, PVC is adopted as the base material with its parameters $E = 2.70$ [GPa] and $\nu = 0.38$ taken from [9].

4.3. Boundary conditions and loads

For the idealized cell-based models, to fulfil the periodicity assumptions, periodic boundary conditions are enforced on both \vec{w}_r and $\vec{\theta}$, i.e. $\vec{w}_r^- = \vec{w}_r^+$ and $\vec{\theta}^- = \vec{\theta}^+$ (see also Section 2). Since no periodicity is present for the tessellation-based models and minimal kinematic boundary conditions is usually too weak (see e.g. [85]), fully prescribed boundary conditions are enforced on \vec{w}_r , i.e. $\vec{w}_r = \vec{0}$ (see also Section 2). This choice is appropriate as long as the RVE dimensions are large enough, which is the case in the present study.

To investigate the anisotropic compressive behavior, uniaxial compressive loadings in different global directions are applied, by prescribing the macroscale effective quantities $(\bar{\mathbf{F}}, \bar{\mathbf{P}})$ in a mixed manner. Loading case \vec{e}_1 is specified below as an example:

$$\hat{\mathbf{F}} = \begin{bmatrix} \lambda & 0 & 0 \\ \times & \times & 0 \\ \times & \times & \times \end{bmatrix}, \quad \hat{\mathbf{P}} = \begin{bmatrix} \times & \times & \times \\ 0 & 0 & \times \\ 0 & 0 & 0 \end{bmatrix}. \quad (38)$$

Here, $\hat{\mathbf{F}}$ and $\hat{\mathbf{P}}$ have been projected to the global basis \vec{e}_i ; λ denotes the prescribed stretch ratio and “ \times ” the unprescribed (unknown) components. Notice that half of the non-diagonal components in $\hat{\mathbf{F}}$ have also been prescribed to eliminate the rigid-body rotation.

The complete RVE problem (33) is implemented by coupling the open-source computing platform FEniCS [94, 95] with MFront [93], where $\hat{\mathbf{F}}$ is treated as global DOF in addition to local DOF \vec{w}_r and $\vec{\theta}$.

5. Analyses of the idealized cell-based models

Numerical results of the idealized cell-based models introduced in Section 4 will be analyzed in this section, to exemplify the anisotropic compressive behavior and deformation mechanisms of closed-cell foams, as well as how different compressive properties evolve with cell shape anisotropy, in absence of any mesostructural stochastics.

5.1. Rectangular parallelepiped cell

The macroscale effective stresses $\hat{\mathbf{P}}$ and strain energy fractions $\hat{W}_p/\hat{W}_{\text{tot}}$ of different deformation modes⁴, for shape anisotropy $\mathcal{R} = 1.5$, are plotted as functions of the applied strain in Figure 5. The effective responses for loading case \vec{e}_2 are identical to those for \vec{e}_1 and thus not displayed. Figure 5(a) shows that for each loading case, the stress first increases linearly, followed by a sudden drop (black crosses). Interestingly, the stress drop appears twice for loading case \vec{e}_1 . Since no plasticity is accounted for, the typical plateau region observed in experiments is not captured. As expected, the stress under compression in the foam rise direction (\vec{e}_3) is much higher than the transverse direction (\vec{e}_1), indicating an anisotropic compressive behavior. Figure 5(b) shows that for each loading direction, the cell structure experiences a nearly pure membrane deformation mode ($\hat{W}^m/\hat{W}_{\text{tot}} \sim 1$) in the initial elastic region, while the bending mode gets pronounced after the stress drop.

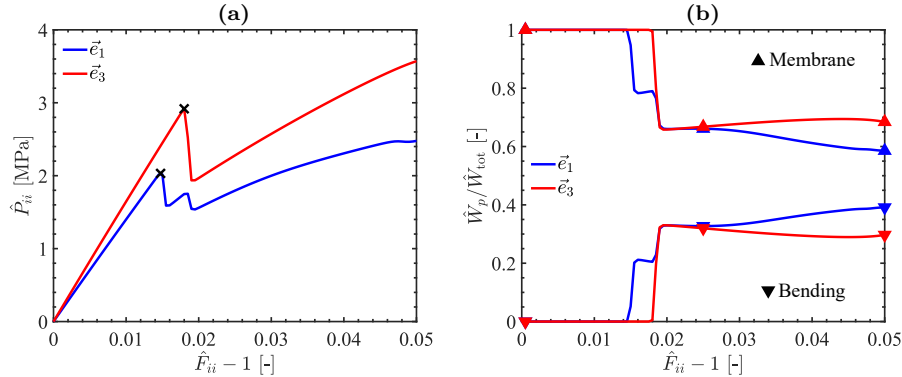


Figure 5: Effective responses of the rectangular parallelepiped cell-based model with $\mathcal{R} = 1.5$, under uniaxial compression in the transverse (\vec{e}_1) and foam rise (\vec{e}_3) directions: (a) stress and (b) strain energy fraction versus applied strain. The yield points are indicated in (a) by the black crosses.

To rationalize the observations in Figure 5, individual cell wall deformation behaviors are quantified using the method introduced in Section 3, with the results reported in Figure 6. The strain energy partitioning indicator \mathcal{I}_w (using eq. (34)) of each cell wall is plotted as a function of the applied strain, and colored by its strain energy contribution percentage. The deformation configurations are colored by the displacement fluctuations for better

⁴The transverse shear contribution has been included in the total strain energy for completeness.

visualization of buckling. Figure 6 shows that only the two cell walls parallel with the loading direction accommodate strain energy. These cell walls deform first by the membrane mode ($\mathcal{I}_w \sim -1$) and then switch to a mixed membrane-bending mode after buckling (black crosses). In particular, under compression in the transverse direction, the larger cell wall buckles earlier than the other one. The cell wall buckling points correspond well with the stress drop points in Figure 5(a)). The results for other shape anisotropy have confirmed similar behavior to those presented for $\mathcal{R} = 1.5$ and are thus not shown here.

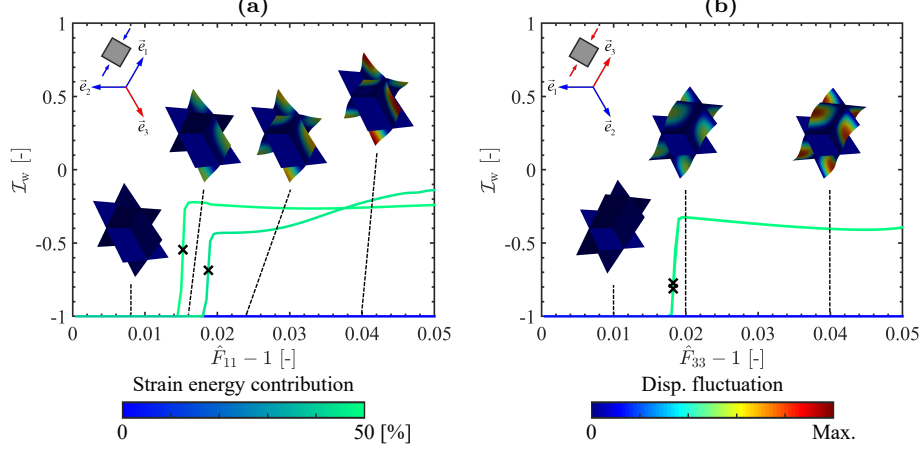


Figure 6: Cell wall strain energy partitioning indicators versus applied strain and deformed configurations at different stages of the rectangular parallelepiped cell-based model with $\mathcal{R} = 1.5$, under uniaxial compression in the (a) transverse and (b) foam rise directions. The two green curves in (b) are overlapping. The loading direction is represented by a pair of opposite arrows. The buckling points are indicated by the black crosses.

Next, the effective compressive properties are extracted and plotted against varying shape anisotropy \mathcal{R} in Figure 7. For each loading direction \vec{e}_i , the compressive modulus and Poisson's ratio are evaluated as $\hat{E}_{ii} = \Delta \hat{P}_{ii} / \Delta \hat{F}_{ii}$ and $\hat{\nu}_{ij} = -\Delta \hat{F}_{jj} / \Delta \hat{F}_{ii}$, respectively, in the initial elastic region. The yield strength is determined by $\hat{\sigma}_{y,ii} = \hat{P}_{ii}$ at the first cell wall buckling point (also indicated in Figure 6(a)). Regarding elastic properties, Figure 7(a) shows that \hat{E}_{33} increases while \hat{E}_{11} decreases with increasing \mathcal{R} , reflecting an increasing modulus ratio $\hat{E}_{33} / \hat{E}_{11}$. Figure 7(b) shows that $\hat{\nu}_{31} = \hat{\nu}_{32}$ for a given \mathcal{R} , as expected for a transverse isotropy. $\hat{\nu}_{13}$ and $\hat{\nu}_{31}$ both increase along with \mathcal{R} while $\hat{\nu}_{12}$ decreases. Compared with $\hat{\nu}_{13}$, $\hat{\nu}_{31}$ presents a stronger dependency on \mathcal{R} . This can be understood through the well-known relation $\hat{\nu}_{13} / \hat{E}_{11} = \hat{\nu}_{31} / \hat{E}_{33}$. To the authors' best knowledge, how the compressive Poisson's ratio evolves with cell shape anisotropy is rarely discussed in the literature.

Back to Figure 7(a), the compressive strength $\hat{\sigma}_{y,33}$ increases as \mathcal{R} increases, while $\hat{\sigma}_{y,11}$ first decreases and then increases slightly. Nevertheless, the resulting strength ratio $\hat{\sigma}_{y,33} / \hat{\sigma}_{y,11}$ implies an overall rising trend with respect to \mathcal{R} . Moreover, a stronger dependency on \mathcal{R} can be observed for $\hat{\sigma}_{y,33} / \hat{\sigma}_{y,11}$, compared with $\hat{E}_{33} / \hat{E}_{11}$.

In addition, the initial stress states and buckling patterns are analyzed. As the cell wall membrane deformation is found to dominate the initial elastic region, the membrane stress triaxiality is evaluated to better understand the stress states prior to buckling. The results for several \mathcal{R} are reported in Figure 8. It can be seen that the initial stress states of the two cell walls for $\mathcal{R} = 1.5$, parallel with the loading direction, are close to uniaxial compression (theoretical triaxiality $-1/3$). Similar stress triaxiality distributions have been confirmed for other shape anisotropy and are thus not presented.

The buckling patterns are visualized through the deformed configurations colored by the normalized displacement fluctuations. For each \mathcal{R} , the initial buckling takes place in the

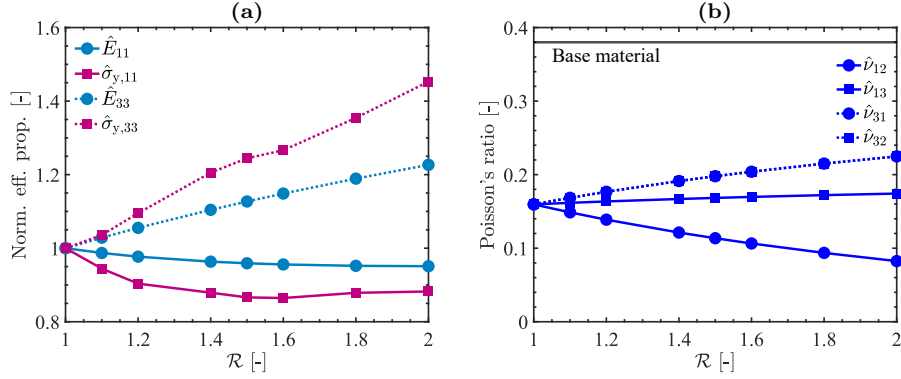


Figure 7: Effective compressive properties of the rectangular parallelepiped cell-based models with different shape anisotropy \mathcal{R} : (a) modulus and yield strength, and (b) Poisson's ratio. Effective properties in (a) have been normalized with respect to those at $\mathcal{R} = 1$. The base material Poisson's ratio is indicated in (b) for reference.

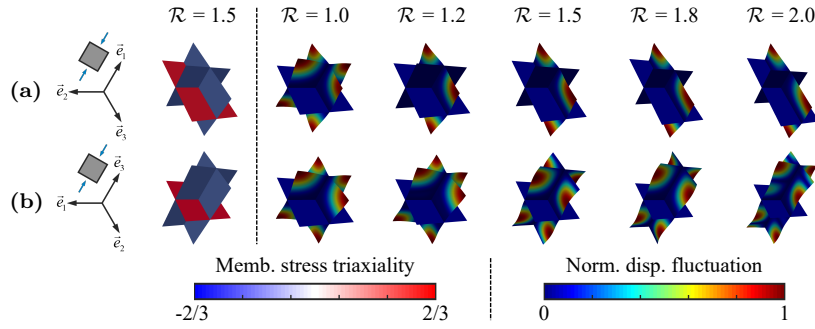


Figure 8: Initial membrane stress triaxialities and buckling patterns of the rectangular parallelepiped cell-based models with different shape anisotropy \mathcal{R} , under uniaxial compression in the (a) transverse and (b) foam rise directions. The practical triaxiality values range from -0.48 to 0.67 in (a), and from -0.43 and 0.67 in (b), respectively. The loading direction is represented by a pair of opposite arrows.

relatively large cell wall which is parallel with the loading direction. The buckling pattern depends on the loading direction as well as \mathcal{R} .

5.2. Kelvin cell

The macroscale effective responses for shape anisotropy $\mathcal{R} = 1.5$ are reported in Figure 9. For each loading case, the initial elastic region is followed by a stiffness reduction (like yielding, see black crosses in Figure 9(a)) rather than a sudden stress drop observed for the rectangular parallelepiped cell (see Figure 5(a)). The compressive stress in the foam rise direction (\vec{e}_3) is well above that in the transverse direction (\vec{e}_1), indicating an anisotropic compressive behavior. The strain energy fraction profiles (see Figure 9(b)) demonstrate that for each loading direction, the membrane deformation mode ($\hat{W}^m/\hat{W}_{\text{tot}} \sim 1$) governs the initial elastic region and the bending mode becomes important only after the stiffness reduction. The corresponding strain energy redistribution proceeds gradually instead of in a sudden manner observed for the rectangular parallelepiped cell (see Figure 5(b)).

The cell wall-wise strain energy partitioning indicators \mathcal{I}_w are reported in Figure 10. It can be seen that the strain energy is mainly accommodated by the eight hexagonal cell walls inclined about the loading direction and the three quadrilateral ones parallel with the loading direction. These cell walls deform first by the membrane mode ($\mathcal{I}_w \sim -1$), followed by transition towards a mixed membrane-bending mode after buckling (black crosses).

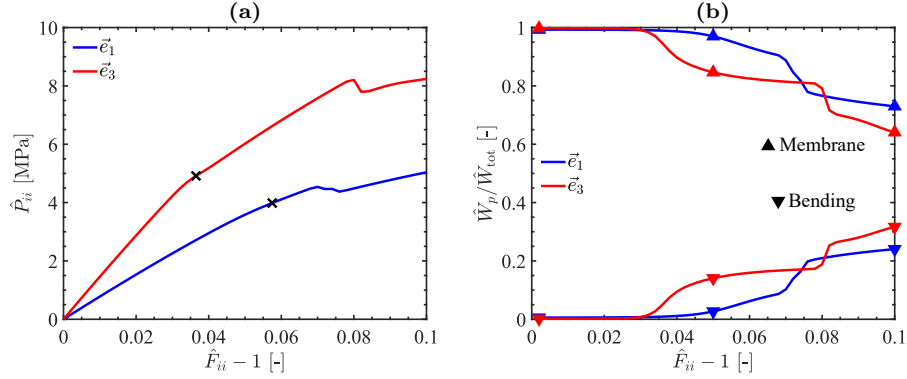


Figure 9: Effective responses of the Kelvin cell-based model with $\mathcal{R} = 1.5$, under uniaxial compression in the transverse (\vec{e}_1) and foam rise (\vec{e}_3) directions: (a) stress and (b) strain energy fraction versus applied strain.

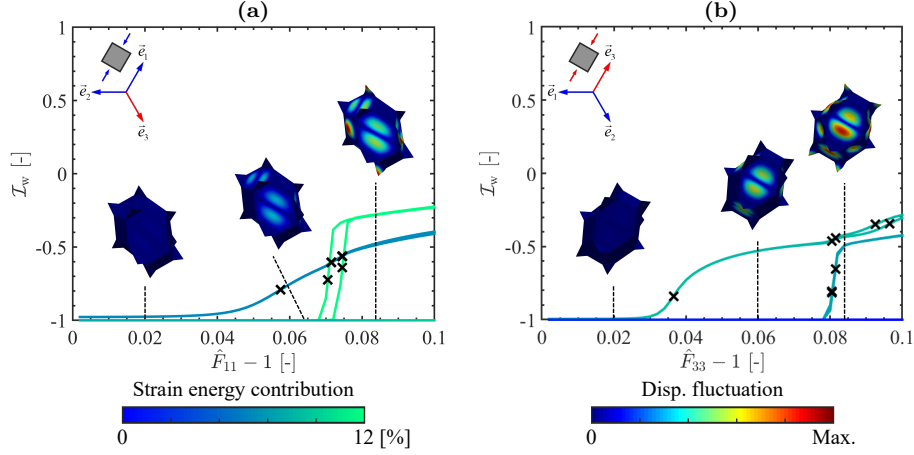


Figure 10: Cell wall strain energy partitioning indicators versus applied strain and deformed configurations at different stages of the Kelvin cell-based model with $\mathcal{R} = 1.5$, under uniaxial compression in the (a) transverse and (b) foam rise directions.

The inclined cell walls present a gradual deformation mode transition in contrast to the parallel ones. This can be explained by that the inclination angle increases with increasing applied strain, leading to a reduction of load portion projected in the cell wall plane.

Besides, the large, inclined cell walls buckle earlier than the small, parallel ones, especially under compression in the foam rise direction. The first set of buckling points of the inclined and parallel cell walls correspond well with the stiffness reduction and stress drop points in Figure 9(a), respectively. Several cell walls experience multiple times of buckling, likely because of the mutual interactions between different types of cell walls that may raise perturbations. Similar observations have been confirmed for other shape anisotropy.

The effective compressive properties for different shape anisotropy \mathcal{R} are reported in Figure 11. As \mathcal{R} increases, the compressive modulus \hat{E}_{33} increases while \hat{E}_{11} decreases (see Figure 11(a)), implying a rapid increase of the modulus ratio $\hat{E}_{33}/\hat{E}_{11}$. The compressive Poisson's ratios $\hat{\nu}_{12}$ and $\hat{\nu}_{31}$ (identical to $\hat{\nu}_{32}$) both increase along with \mathcal{R} while $\hat{\nu}_{13}$ decreases (see Figure 11(b)).

The compressive strength $\hat{\sigma}_{y,33}$ increases along with \mathcal{R} , while $\hat{\sigma}_{y,11}$ remains almost constant, leading to a slow increase of the strength ratio $\hat{\sigma}_{y,33}/\hat{\sigma}_{y,11}$ (see Figure 11(a)). Compared with $\hat{E}_{33}/\hat{E}_{11}$, $\hat{\sigma}_{y,33}/\hat{\sigma}_{y,11}$ is much less sensitive to \mathcal{R} .

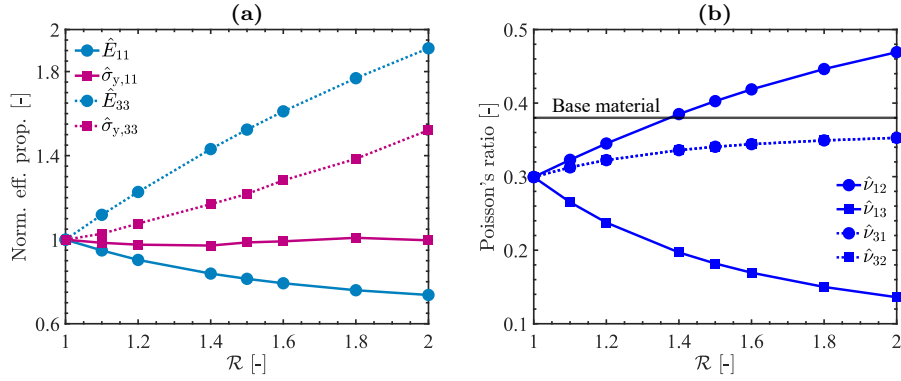


Figure 11: Effective compressive properties of the Kelvin cell-based models with different shape anisotropy \mathcal{R} : (a) modulus and yield strength, and (b) Poisson's ratio.

The initial membrane stress triaxialities and buckling patterns for several \mathcal{R} are reported in Figure 12. Nearly uniaxial compression stress states can be observed on the eight inclined and three parallel cell walls with respect to the loading direction. Similar stress states have also been confirmed for Kelvin cells with other shape anisotropy.

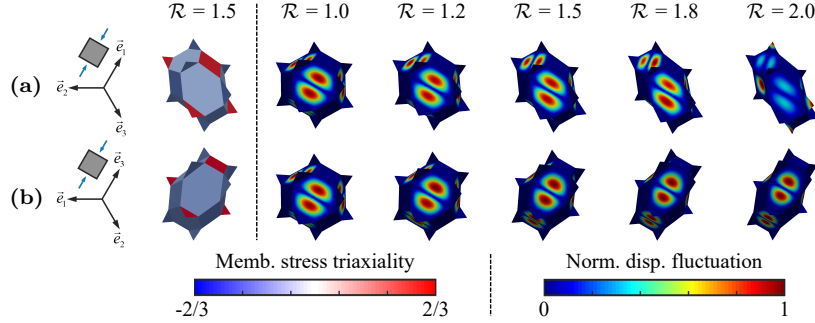


Figure 12: Initial membrane stress triaxialities and buckling patterns of the Kelvin cell-based models with different shape anisotropy \mathcal{R} , under uniaxial compression in the (a) transverse and (b) foam rise directions. The practical triaxiality values range from -0.44 to 0.64 in (a), and from -0.36 and 0.67 in (b), respectively.

For each \mathcal{R} , the initial buckling is mainly determined by those large cell walls despite being inclined, especially under compression in the foam rise direction. Again, different buckling patterns can be seen for different loading directions and \mathcal{R} .

5.3. Discussion

Despite numerous simplifications, the idealized cell-based models have shown capabilities to qualitatively reproduce the anisotropic compressive behavior of realistic foams. Through quantitative analysis of the cell wall deformation behavior, a few preliminary insights into the deformation mechanisms can be summarized:

1. The initial elastic region is primarily governed by the cell wall membrane deformation, regardless of the loading direction.
2. The cell wall bending contribution becomes crucial only after foam yielding.

Notice that the first insight has been raised to some extent elsewhere (see e.g. [44, 45, 61]), however, limited to isotropic foams and lacking confirmation of the cell wall deformations. It will be shown in Section 7 that these insights hold even when the mesostructural stochastics are taken into account. Accordingly, the anisotropic compressive properties of the foams

with a high cell face fraction, as considered in this study, may not be simply explained by different deformation mechanisms for different loading directions, in contrast to those with a low cell face fraction (see [Section 1](#)).

Besides, the Kelvin cells exhibit distinctly different anisotropy trends of compressive properties from the rectangular parallelepiped cells. Extensive experimental observations on Divinycell foams (see e.g. [\[27, 7, 9\]](#)) have confirmed that, compared with the modulus anisotropy, the strength anisotropy is much less sensitive to shape anisotropy. This trend can be captured by the Kelvin cell but not by the rectangular parallelepiped cell. All the above suggest that the cell wall inclination angle has non-negligible impacts on the mechanical anisotropy of realistic foams, in addition to the primary role of cell shape anisotropy.

6. Relationships between mechanical anisotropy and cell shape anisotropy

The insights obtained in [Section 5](#) will guide derivations of analytical models in this section, to illustrate how cell shape anisotropy translates into mechanical anisotropy.

6.1. Model development

6.1.1. Rectangular parallelepiped cell

In a rectangular parallelepiped cell structure, the cell walls parallel with the loading direction constitute the primary load-bearing elements (see [Figure 6](#)), as sketched in [Figure 13\(a\)](#). The cell length and cross-section area in the loading direction are indicated by L and A , respectively. For instance, under compression in the foam rise direction \vec{e}_3 (see [Figure 4\(a\)](#)), $L = L_3$ and $A = L_1 L_2$. The cell wall length spans over the entire cell, i.e. $L_w = L$, and the width is indicated by B_w .

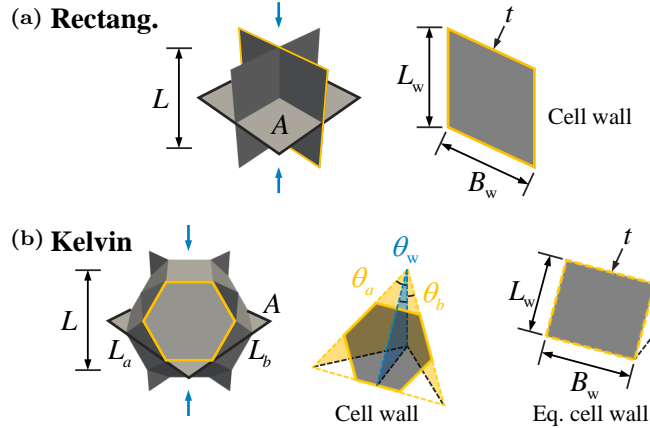


Figure 13: Sketches of the two idealized cell structures and load-bearing cell walls under compression: (a) rectangular parallelepiped and (b) Kelvin cells. The loading direction is represented by a pair of opposite arrows.

By assuming an iso-strain condition, the effective compressive modulus \hat{E} can be expressed as:

$$\hat{E} = \frac{L}{A} \sum^N K_w, \quad (39)$$

with N being the number of load-bearing cell walls and K_w the cell wall-wise membrane stiffness given by

$$K_w \propto \frac{t}{L} B_w, \quad (40)$$

where a uniaxial compression stress state (see Figure 8) has been assumed; “ \propto ” represents a proportional relationship.

The effective compressive strength in the loading direction can be expressed as:

$$\hat{\sigma}_y = \frac{\min\{\sigma_{c,w}\}t}{A} \sum^N B_w, \quad (41)$$

with $\sigma_{c,w}$ the cell wall-wise buckling stress. Note, that $\hat{\sigma}_y$ is determined by the weakest cell wall, i.e. with the lowest aspect ratio $\mathcal{R}_w = L_w/B_w$ (see Figure 8). Following the rectangular plate buckling theory (see e.g. [96]), $\sigma_{c,w}$ is given by

$$\sigma_{c,w} \propto k_c \left(\frac{t}{B_w} \right)^2, \quad (42)$$

with k_c the buckling coefficient which depends on \mathcal{R}_w . Although the exact solutions for k_c are available only under certain boundary conditions, the functional form below provides a sufficient approximation in most cases (see also [96])

$$k_c \propto \mathcal{K}_c(\mathcal{R}_w) = 1 - k + k(\mathcal{R}_w)^p, \quad (43)$$

where a normalized buckling coefficient function \mathcal{K}_c with $\mathcal{K}_c(1) = 1$ has been introduced; k and p are the two parameters which can be identified using numerical results.

Using the effective compressive properties ($\hat{E}_{11}, \hat{E}_{33}$) and ($\hat{\sigma}_{y,11}, \hat{\sigma}_{y,33}$) in the transverse (\vec{e}_1) and foam rise (\vec{e}_3) directions, which are given by eqs. (39) and (41), the modulus anisotropy \mathcal{R}^E and strength anisotropy \mathcal{R}^σ for rectangular parallelepiped cell, can be expressed as:

$$\mathcal{R}^E = \frac{\hat{E}_{33}}{\hat{E}_{11}} = \mathcal{R}_f, \quad (44a)$$

$$\mathcal{R}^\sigma = \frac{\hat{\sigma}_{y,33}}{\hat{\sigma}_{y,11}} = \mathcal{R}_c \mathcal{R}_f, \quad (44b)$$

where \mathcal{R}_f denotes a cell load-bearing area fraction ratio and \mathcal{R}_c a cell wall buckling stress ratio, defined through

$$\mathcal{R}_f = \frac{\{f_w\}_3}{\{f_w\}_1}, \quad \mathcal{R}_c = \frac{\min\{\sigma_{c,w}\}_3}{\min\{\sigma_{c,w}\}_1}, \quad (45)$$

with $f_w = \frac{t}{A} \sum B_w$. It can be seen that \mathcal{R}^E is purely determined by \mathcal{R}_f , while \mathcal{R}^σ depends on both \mathcal{R}_c and \mathcal{R}_f .

Based on the geometrical relationships shown in Figure 13(a) that allow for expressing L , A and B_w in terms of L_i , followed by substituting $L_1 = L_2 = V^{\frac{1}{3}} \mathcal{R}^{-\frac{1}{3}}$ and $L_3 = V^{\frac{1}{3}} \mathcal{R}^{\frac{2}{3}}$ (see Section 4) into eq. (45), the two ratios \mathcal{R}_f and \mathcal{R}_c can be directly related to shape anisotropy \mathcal{R} through:

$$\mathcal{R}_f = \frac{2\mathcal{R}}{1 + \mathcal{R}}, \quad \mathcal{R}_c = \frac{\mathcal{K}_c(\mathcal{R})}{\mathcal{K}_c(\mathcal{R}^{-1})} \mathcal{R}^2. \quad (46)$$

Combining eqs. (44) and (46), the mechanical anisotropy for rectangular parallelepiped cell can be fully predicted with shape anisotropy as the input.

6.1.2. Kelvin cell

In a Kelvin cell structure, the cell walls inclined about the loading direction may be regarded as the primary load-bearing elements (see Figure 10), as sketched in Figure 13(b). The cell wall inclination angle is indicated by θ_w , which can be related to the two cell edge

inclination angles θ_a and θ_b through

$$\frac{1}{\tan^2 \theta_w} = \frac{1}{\tan^2 \theta_a} + \frac{1}{\tan^2 \theta_b}, \quad (47)$$

with θ_a and θ_b given by

$$\tan \theta_a = \frac{L_a}{L}, \quad \tan \theta_b = \frac{L_b}{L}, \quad (48)$$

where L_a and L_b are the two cell global dimensions on the plane perpendicular to the loading direction. For instance, under compression in the transverse direction \vec{e}_1 (see Figure 4(b)), $L_a = L_2$ and $L_b = L_3$. To continue the analytical model derivations, the hexagonal cell wall is then approximated using an equivalent rectangular cell wall with its length $L_w = \frac{1}{2}L/\cos \theta_w$ and width $B_w = \frac{1}{2}\kappa_w\sqrt{L_a^2 + L_b^2}$; $\kappa_w = \frac{\sqrt{3}}{2}$ is a correction factor such that the equivalent cell wall aspect ratio $\mathcal{R}_w = L_w/B_w = 1$ at $\mathcal{R} = 1$.

Taking into account θ_w , the effective compressive modulus can be expressed by modifying eq. (39) as:

$$\hat{E} = \cos^2 \theta_w \frac{L}{A} \sum \frac{N/2}{2} K_w, \quad (49)$$

where $\cos^2 \theta_w$ represents the membrane stiffness portion of an inclined wall in the loading direction (see also [42]), and the equivalent cell wall membrane stiffness K_w is given by substituting $L_w = \frac{1}{2}L/\cos \theta_w$ into eq. (40)

$$K_w \propto 2 \cos \theta_w \frac{t}{L} B_w. \quad (50)$$

Similarly, the effective compressive strength is expressed by modifying eq. (41) as:

$$\hat{\sigma}_y = \cos \theta_w \frac{\min\{\sigma_{c,w}\}t}{A} \sum^N B_w, \quad (51)$$

where $\cos \theta_w$ represents the membrane stress portion of an inclined wall in the loading direction (see also [42]), and $\sigma_{c,w}$ is already given by eq. (42).

Using the effective compressive properties $(\hat{E}_{11}, \hat{E}_{33})$ and $(\hat{\sigma}_{y,11}, \hat{\sigma}_{y,33})$ in the transverse (\vec{e}_1) and foam rise (\vec{e}_3) directions, which are given by eqs. (49) and (51), \mathcal{R}^E and \mathcal{R}^σ for Kelvin cell, can be expressed as:

$$\mathcal{R}^E = \frac{\hat{E}_{33}}{\hat{E}_{11}} = \mathcal{R}_\theta^3 \mathcal{R}_f, \quad (52a)$$

$$\mathcal{R}^\sigma = \frac{\hat{\sigma}_{y,33}}{\hat{\sigma}_{y,11}} = \mathcal{R}_\theta \mathcal{R}_c \mathcal{R}_f, \quad (52b)$$

where \mathcal{R}_f and \mathcal{R}_c are already defined in eq. (45); the third ratio \mathcal{R}_θ has been introduced

$$\mathcal{R}_\theta = \frac{\cos\{\theta_w\}_3}{\cos\{\theta_w\}_1}. \quad (53)$$

Here, $\{\theta_w\}_i$ is the cell wall inclination angle with respect to the global direction \vec{e}_i (see eq. (47)). It can be seen that for the Kelvin cell, both \mathcal{R}^E and \mathcal{R}^σ are additionally influenced by θ_w through \mathcal{R}_θ , compared with the rectangular parallelepiped cell (see eq. (44)).

Expressing θ_w , L , A and B_w in terms of L_i according to the geometrical relationships shown in Figure 13(b), in combination with $L_1 = L_2 = V^{\frac{1}{3}}\mathcal{R}^{-\frac{1}{3}}$ and $L_3 = V^{\frac{1}{3}}\mathcal{R}^{\frac{2}{3}}$ (see also

Section 4), the three ratios \mathcal{R}_θ , \mathcal{R}_f and \mathcal{R}_c become:

$$\mathcal{R}_\theta = \frac{\sqrt{2}\mathcal{R}}{(1 + \mathcal{R}^2)^{\frac{1}{2}}}, \quad \mathcal{R}_f = \frac{\sqrt{2}\mathcal{R}}{(1 + \mathcal{R}^2)^{\frac{1}{2}}}, \quad \mathcal{R}_c = \frac{\mathcal{K}_c \left(\frac{1}{\sqrt{3}}(1 + 2\mathcal{R}^2)^{\frac{1}{2}} \right)}{\mathcal{K}_c \left(\frac{2}{\sqrt{3}} \frac{(1+2\mathcal{R}^2)^{\frac{1}{2}}}{1+\mathcal{R}^2} \right)} \frac{1 + \mathcal{R}^2}{2}. \quad (54)$$

Notice that \mathcal{R}_θ and \mathcal{R}_f essentially represent different factors despite the same expression. Combining eqs. (52) and (54), the mechanical anisotropy for Kelvin cell can be fully predicted with shape anisotropy as the input.

The above expressions (44a) and (52a) derived for the compressive modulus anisotropy are parameter-free. The use of the compressive strength anisotropy expressions (44b) and (52b) requires parameter identification for the normalized buckling coefficient function (43), which depends on the specific geometry and boundary conditions of the load-bearing cell walls.

6.2. Model assessment

6.2.1. Rectangular parallelepiped cell

To identify the parameters k and p for the function $\mathcal{K}_c(R_w)$ (see eq. (43)), the normalized buckling coefficients of the load-bearing cell walls are extracted (using eqs. (41) and (42)) from numerical simulations for all considered shape anisotropy values \mathcal{R} and loading cases, and plotted in Figure 14(a) against the aspect ratio R_w . The model fit with $k = 0.3277$ and $p = -2.3892$ is shown in Figure 14(a), which well reproduces all the numerical data and almost overlaps with the exact solution with fully clamped boundary conditions [96].

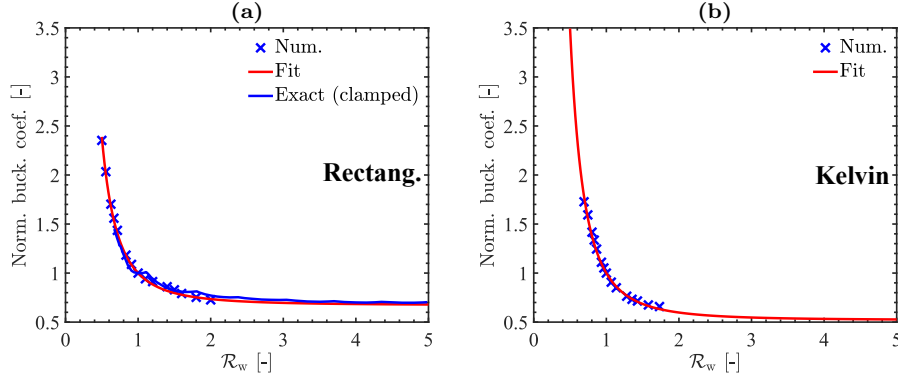


Figure 14: Normalized buckling coefficients versus aspect ratios R_w of the weakest cell walls of the two idealized cell-based models: (a) rectangular parallelepiped and (b) Kelvin cells. Comparison between the numerical data and the model fit is shown. The exact solution with fully clamped boundary conditions [96] are provided in (a) for reference.

To demonstrate the predictive capabilities of the present analytical model, the mechanical anisotropy \mathcal{R}^E and \mathcal{R}^σ computed using eq. (44), are plotted in Figure 15(a) as functions of \mathcal{R} and compared to those from numerical simulations. An excellent agreement can be observed between the numerical data and analytical model predictions. \mathcal{R}^E and \mathcal{R}^σ both increase along with \mathcal{R} , and \mathcal{R}^σ develops faster than \mathcal{R}^E (see also Figure 7(a)).

Moreover, the cell load-bearing area fraction ratio \mathcal{R}_f and cell wall buckling stress ratio \mathcal{R}_c computed using eq. (46), are reported in Figure 15(c). It can be seen that \mathcal{R}_f and \mathcal{R}_c both increase along with \mathcal{R} . According to eq. (44), \mathcal{R}^σ additionally depends on \mathcal{R}_c compared with \mathcal{R}^E , thus resulting in faster development of \mathcal{R}^σ than \mathcal{R}^E , as reflected in Figure 15(a).

In addition, the widely used Gibson-Ashby model [32] is assessed, which is also derived by assuming a rectangular parallelepiped cell structure. Detailed expressions of this reference

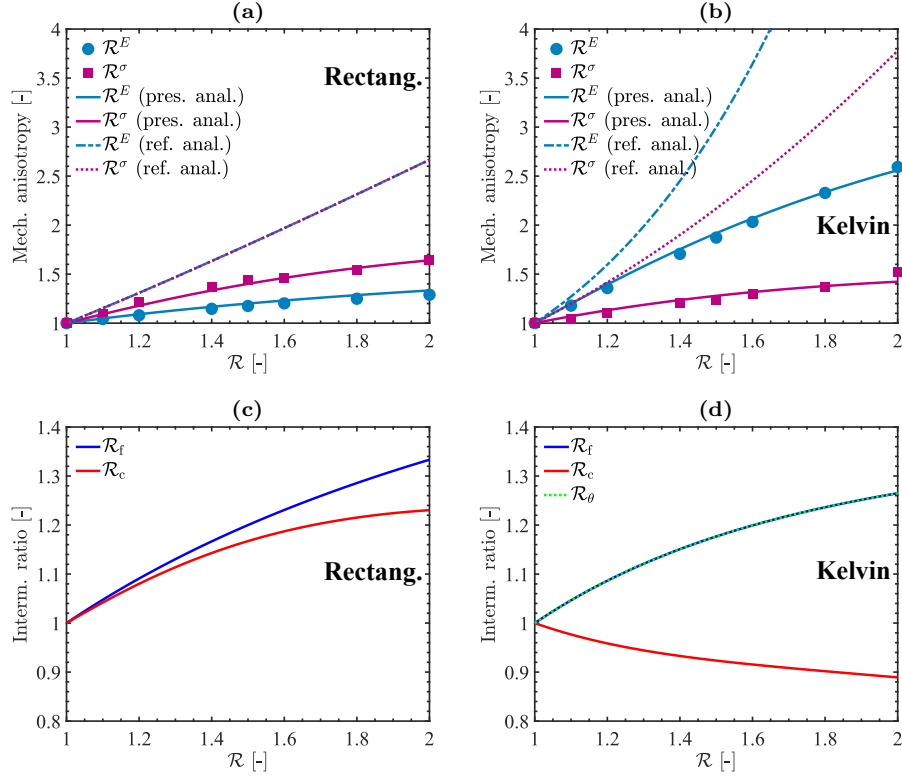


Figure 15: (a-b) Mechanical anisotropy and (c-d) intermediate ratios versus shape anisotropy \mathcal{R} of the two idealized cell-based models: (a,c) rectangular parallelepiped and (b,d) Kelvin cells. Comparison between the numerical data, and predictions by the present (44, 52) and reference [32, 34] analytical models is shown in (a-b).

analytical model can be found in [Appendix C](#) and the corresponding model predictions are reported in Figure 15(a). It can be seen that the Gibson-Ashby model overestimates the mechanical anisotropy, especially modulus anisotropy, by $> 100\%$. Since the same geometrical assumptions have been adopted, these deviations can only be associated with the introduced mechanistic assumptions, i.e. load-bearing cell walls are subjected to a tensile stress state under compression and plastic collapse dominates the compressive failure, that are likely inappropriate at a high cell face fraction and low relative density.

6.2.2. Kelvin cell

To identify the parameters for the function $\mathcal{K}_c(R_w)$, the normalized buckling coefficients extracted (using eqs. (51) and (42)) from numerical simulations, are reported in Figure 14(b). The model fit with $k = 0.4798$ and $p = -2.6315$ for the function $\mathcal{K}_c(R_w)$ is shown in Figure 14(b), which again accurately reproduces all the numerical data.

The mechanical anisotropy \mathcal{R}^E and \mathcal{R}^σ computed using eq. (52) are reported in Figure 15(b), together with those obtained from numerical simulations. Once more, the analytical model predictions agree well with the numerical data. \mathcal{R}^E and \mathcal{R}^σ both increase along with \mathcal{R} , and \mathcal{R}^E develops much faster than \mathcal{R}^σ (see also Figure 11(a)), which is opposite to the trend observed for the rectangular parallelepiped cell (see Figure 15(a)). Moreover, for a given \mathcal{R} , the Kelvin cell has a much higher \mathcal{R}^E while slightly lower \mathcal{R}^σ , than the rectangular parallelepiped cell.

The intermediate ratios \mathcal{R}_f , \mathcal{R}_c and \mathcal{R}_θ computed using eq. (54) are reported in Figure 15(d). \mathcal{R}_f and \mathcal{R}_θ increases along with \mathcal{R} , while \mathcal{R}_c slightly decreases. According to

eq. (52), \mathcal{R}^E has a cubic dependency on \mathcal{R}_θ while \mathcal{R}^σ a linear dependency, leading to much faster development of \mathcal{R}^E than \mathcal{R}^σ , as shown in Figure 15(b). Interestingly, comparing Figures 15(c) and (d) indicates that the curve $\mathcal{R}_f(\mathcal{R})$ for the Kelvin cell is similar to that for the rectangular parallelepiped cell. The curves $\mathcal{R}_c(\mathcal{R})$ for the two idealized cell structures are however completely different, which may be related to different shapes of their load-bearing cell walls. Due to the additional strong dependency on \mathcal{R}_θ , the curve $\mathcal{R}^E(\mathcal{R})$ for the Kelvin cell (see Figure 15(b)) is well above that for the rectangular parallelepiped cell (see Figure 15(a)).

For the sake of assessment, the predictions by another widely used analytical model, Sullivan model [34], are reported in Figure 15(b). Detailed expressions of this reference model are given in Appendix C. Despite being applied for closed-cell foams in many studies, the Sullivan model is derived by assuming an open Kelvin cell structure, which is in principle inappropriate for closed-cell foams with a high cell face fraction. As expected, large deviations can be observed on the Sullivan model predictions, especially for the strength anisotropy, which is overestimated by $> 200\%$.

6.3. Discussion

The present analytical models have shown capabilities to accurately reproduce the mechanical anisotropy obtained from the idealized cell-based numerical models. Detailed analysis on the impacts of cell shape anisotropy indicates that:

- Cell shape anisotropy translates into mechanical anisotropy through three pathways, cell load-bearing area fraction, cell wall buckling stress and cell wall inclination angle.
- The inclination angle plays a critical role in determining mechanical anisotropy, in particular modulus anisotropy.

The specific relationships between mechanical anisotropy and cell shape anisotropy would vary from one case to another, depending on the competition among the three pathways above.

In addition, two widely used analytical models [32, 34] exhibit large predictive deviations already for the idealized cell structures, where consistent geometrical assumptions are adopted. These deviations are believed to originate from the introduced mechanistic assumptions, which appear to be inappropriate for closed-cell foams with a high cell face fraction and low relative density. This explains why the predictive capabilities of these analytical models for realistic foams can sometimes be quite low (see e.g. [35, 36, 27, 9]).

7. Analyses of the tessellation-based models

Numerical results of the tessellation-based models incorporating different mesostructural stochastics, will be analyzed in this section.

7.1. Deformation mechanisms

The macroscale effective responses of the model set “StSt” for Divinycell foam H100 and H200, which account for the stochastic variations of cell size, cell wall thickness and cell shape anisotropy, are reported in Figure 16. As expected, the effective responses in two transverse directions (\bar{e}_1/\bar{e}_2) are quite close. Figure 16(a) shows that for each loading case of H100, the stress first increases linearly, followed by a continuous stiffness reduction. The compressive stress in the foam rise direction (\bar{e}_3) is higher than the transverse direction (\bar{e}_1/\bar{e}_2), indicating an anisotropic compressive behavior. Figure 16(c) shows that for each loading direction, the initial elastic region is dominated by the membrane deformation mode ($\hat{W}^m/\hat{W}_{\text{tot}} > 0.95$), followed by a continuous increase of the bending contribution. Similar

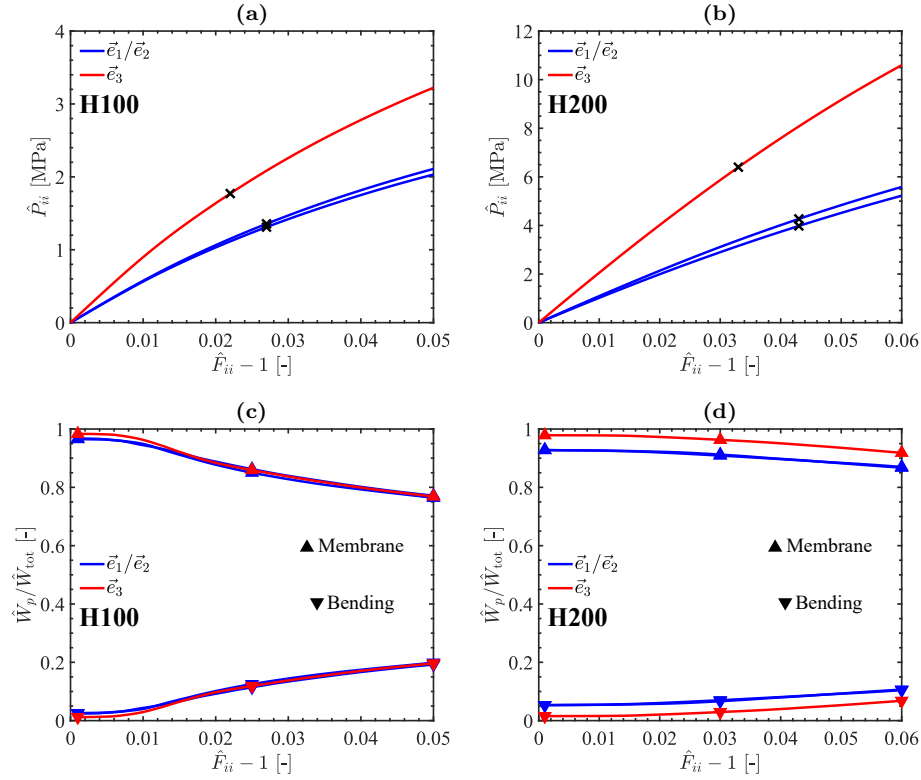


Figure 16: (a-b) Effective stresses and (c-d) strain energy fractions versus applied strain of the tessellation-based model set “StSt” for two Divinycell foam grades, under uniaxial compression in the transverse (\vec{e}_1/\vec{e}_2) and foam rise (\vec{e}_3) directions. The yield points are indicated in (a-b) by the black crosses, which are determined at the experimental yield strains for H100 [97] and H200 [98], respectively.

trends can be observed for H200 from Figures 16(b) and (d). Yet, the stiffness reduction is less pronounced, and the bending contribution increase rate is lower than H100.

To interpret the observations in Figure 16, cumulative density functions (CDF) of the cell wall strain energy partitioning indicators at different applied strains, are reported in Figure 17. Figures 17(a) and (c) demonstrate that $> 80\%$ and $> 90\%$ of cell walls of H100 deform by a nearly pure membrane mode ($\mathcal{I}_w < -0.8$) at the early stage, under compression in the transverse and foam rise directions, respectively. As the loading increases, more and more cell walls buckle and switch to a mixed membrane-bending mode. Attributed to the large variations of cell size and cell wall thickness (see Table 2), the buckling resistance greatly varies between individual cell walls, leading to sequential occurrence of buckling and thus gradual energy redistribution in Figure 16(c). This holds for both the transverse and foam rise directions.

Figures 17(b) and (d) for H200 demonstrate similar trends as those for H100. However, fewer cell walls buckle, resulting in slower deformation mode transition compared with H100. This can be understood by the larger cell wall thickness of H200 (see Table 2), which gives rise to a higher buckling resistance. Numerical simulations on “StCt” and “CtCt” have delivered qualitatively similar results as “StSt” and are thus omitted here.

The above analyses confirm that the deformation mechanisms identified using the idealized cell structures (see Section 5) remain valid in the presence of mesostructural stochasticity.

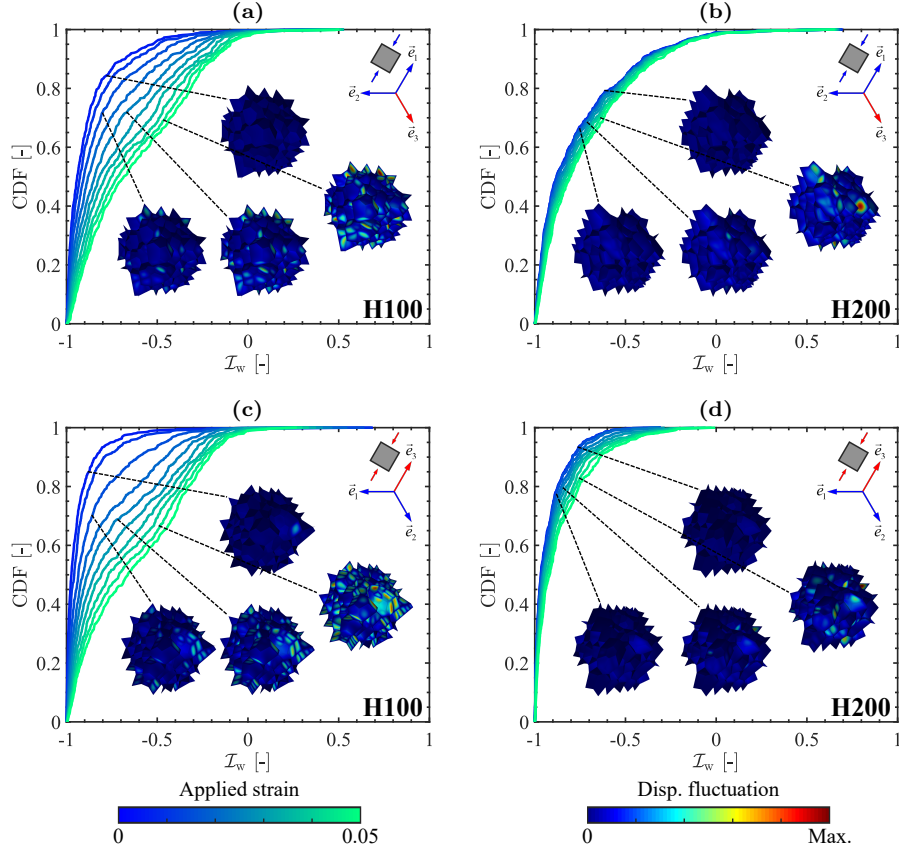


Figure 17: Cumulative density functions (CDF) of the cell wall strain energy partitioning indicators and deformed configurations at different stages of the tessellation-based model set “StSt” for two Divinycell foam grades, under uniaxial compression in the (a-b) transverse and (c-d) foam rise directions. The loading direction is represented by a pair of opposite arrows.

7.2. Effective properties

The effective compressive properties of different model sets are reported in Figure 18. As there are neither apparent stress drop points nor apparent start points of stress reduction visible on the numerical stress-strain curves (see Figures 16(a) and (b)), the yield strengths are determined using a strain-based method instead. The yield strains $\hat{\varepsilon}_{y,ii}$ of H100 and H200, are taken at the peak stress points of the experimental stress-strain curves in [97] and [98], respectively. The specific values are $\hat{\varepsilon}_{y,11} = \hat{\varepsilon}_{y,22} = 0.027$ and $\hat{\varepsilon}_{y,33} = 0.022$ for H100 (also indicated in Figure 16(a)), and $\hat{\varepsilon}_{y,11} = \hat{\varepsilon}_{y,22} = 0.043$ and $\hat{\varepsilon}_{y,33} = 0.033$ for H200 (also indicated in Figure 16(b)), respectively.

Comparing the results of different model sets for H100 in Figures 18(a) and (c) shows that for each loading direction, as the stochastic variations of cell size and cell wall thickness are sequentially incorporated (from “CtCt” to “StSt”), the compressive modulus and strength both decrease, while the Poisson’s ratios remain almost unchanged. Compared with the compressive modulus, the strength is more sensitive to these mesostructural stochastics. Similar trends can be observed for H200 from Figures 18(b) and (d). Given the higher relative density of H200 (see Table 2), the resulting compressive moduli and strengths are apparently higher than H100. Interestingly, the Poisson’s ratios of H100 and H200 are quite similar despite their distinct mesostructures.

Nevertheless, one should be careful with interpreting the impacts of cell size stochastics.

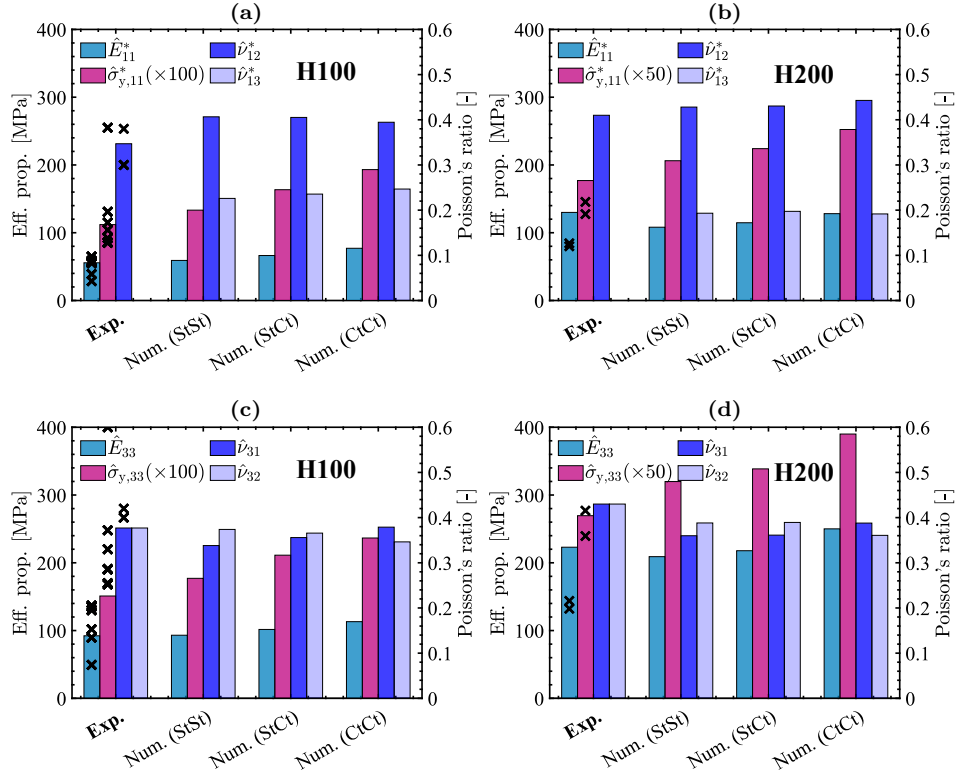


Figure 18: Effective compressive properties of different tessellation-based model sets for two Divinycell foam grades. (●)* in (a-b) indicates the average of quantities in two transverse directions (\bar{e}_1/\bar{e}_2). Experimental data collected from extensive literature are provided for reference. H100 data from [97] and H200 data from [98] are indicated by the leftmost bars. H100 data from [99, 100, 101, 27, 98, 102, 103] and H200 data from [27, 104] are indicated by the black crosses.

Based on empirical relationships between the compressive properties and relative density for closed-cell foams [8], the net impacts of cell size stochastics may be secondary in practice. When analyzing the model sets for each Divinycell foam grade, the resulting overall relative density ρ/ρ_r of “CtCt” is $\sim 10\%$ higher than those of “StSt” and “StCt” (see Section 4). At the same time, the compressive properties of “CtCt” is $\sim 15\%$ higher than “StCt” (see Figures 18). It is thereby likely that this difference in compressive properties is primarily related to the change in ρ/ρ_r rather than to the change in cell size stochastics. To examine this inference, numerical simulations of “CtCt” H100 and H200, with the cell wall thickness scaled such that the the resulting ρ/ρ_r are equal to those of “StCt”, are performed. The resulting compressive moduli and strengths of the scaled “CtCt” are found to be quite close to those of “StCt”, with a relative difference $< 5\%$. This confirms that the compressive properties receive secondary impacts from the cell size stochastics in practice, despite being still noticeable⁵.

⁵More pronounced impacts by the cell size stochastics are claimed in other numerical studies [65, 66], which focus on Gurit Corecell foam M130, nearly isotropic. Mesosstructural models with different cell size distributions while the relative density preserved, are considered. With a cell size distribution comparable to the present study, the resulting compressive modulus and strength are found to decrease by $\sim 5\%$ and $\sim 10\%$, respectively, compared to the case with a constant cell size. However, the overall cell equivalent diameter is not preserved and increases along with increasing cell size stochastic variations. This would already weaken especially the compressive strength. Therefore, we believe that the net impacts of cell size stochastics is less pronounced than being claimed in [65, 66].

The above observed decreasing trends of compressive properties with increasing mesostructural stochastics can be explained through the weakest link principle (see also [61, 62]). Introducing the stochastic variations of more mesostructural features gives rise to the emergence of more weak regions. Indeed, Figure 19 demonstrates that the cell wall buckling events (using eq. (36)) tend to get promoted as more mesostructural stochastics are included (from “CtCt” to “StSt”). Here, N_c and N_w denote the number of buckled cell walls and the total number of cell walls, respectively. The fractions N_c/N_w of buckled cell walls for different model sets eventually become comparable upon a large applied strain. As expected, the cell wall buckling events for H200 are postponed (see also Figure 17) and accompanied by a slower growth of N_c/N_w , compared with H100.

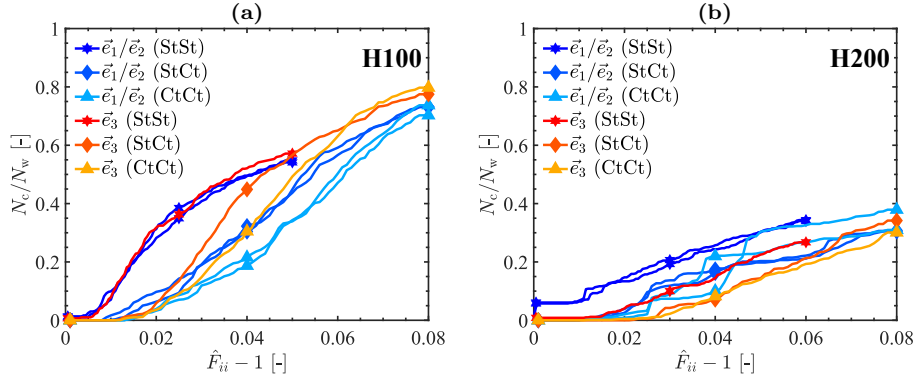


Figure 19: Fractions of buckled cell walls versus applied strain of different tessellation-based model sets for two Divinycell foam grades, under uniaxial compression in the transverse (\vec{e}_1/\vec{e}_2) and foam rise (\vec{e}_3) directions.

For the sake of reference, the experimental compressive properties of H100 [97] and H200 [98], are provided in Figure 18 (leftmost bars). $\hat{\nu}_{13}^*$ are not measured and $\hat{\nu}_{31} = \hat{\nu}_{32}$ has been assumed in [97, 98]. As an indication, the experimental data from other literature are also provided in Figure 18 (black crosses), although these studies are lacking either well-defined strain measurements or complete stress-strain curves under uniaxial compression. A remarkable inconsistency between the experimental data reported in different literature can be noticed. This places a clear need of more attention to the experimental aspects, e.g. test method, sample shape, sample size and determination of compressive properties.

In the following, the numerical model predictions are compared with the experimental data from [97, 98] only, given their reliability and relevance. The model set “StSt”, with all the cell size, cell wall thickness and cell shape anisotropy stochastics incorporated, seems to deliver the closest predictions with respect to the experimental data. In particular for the compressive moduli and Poisson’s ratios, an excellent agreement between the experimental data and “StSt” predictions can be observed. Relatively large deviations appear on the strengths, which are overestimated by $\sim 15\%$, likely due to the disregarded plasticity in the present numerical models.

7.3. Mechanical anisotropy

With the effective compressive properties in Figure 18, the mechanical anisotropy \mathcal{R}^E and \mathcal{R}^σ of different model sets are computed, and reported in Figures 20(a) and (b), respectively. Three model sets (“StSt”, “StCt” and “CtCt”), are found to deliver comparable predictions of both \mathcal{R}^E and \mathcal{R}^σ , with the relative difference in between $< 10\%$. This suggests that the cell wall thickness and cell size stochastics only weakly affect the resulting mechanical anisotropy.

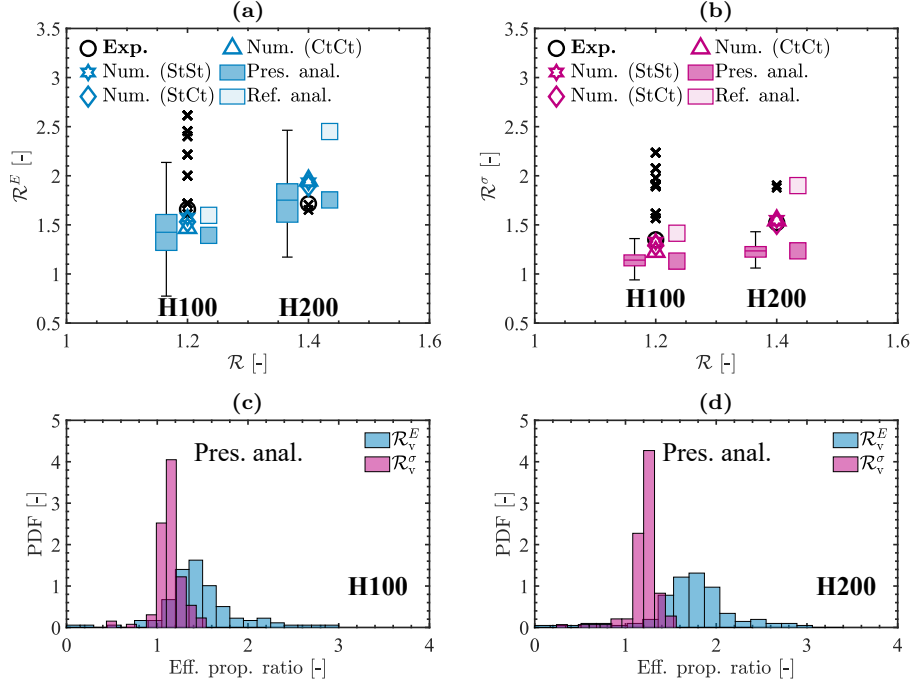


Figure 20: Mechanical anisotropy predicted by different tessellation-based numerical models, and the idealized cell-based present (52) and reference [34] analytical models for two Divinycell foam grades: (a) modulus and (b) yield strength; (c-d) probability density functions (PDF) of the cell mechanical anisotropy computed using the present analytical model (52). The analytical model predictions and the five-number summary statistics in (a-b) are shifted horizontally for better visibility. Experimental data collected from extensive literature are provided in (a-b) for reference. H100 data from [97] and H200 data from [98] are indicated by the black circles. H100 data from [99, 100, 101, 27, 98, 102, 103] and H200 data from [27, 104] are indicated by the black crosses.

Again, \mathcal{R}^E and \mathcal{R}^σ computed using the experimental data in Figure 18, are supplemented to Figures 20(a) and (b), respectively (black markers). It seems that the experimental mechanical anisotropy (black circles) from [97, 98], especially strength anisotropy, can be well reproduced using any of the three model sets. Nevertheless, given the large inconsistency among the experimental data from different literature (see also Figure 18), it is hardly feasible to conduct in-depth analysis regarding the accuracy of model predictions.

In order to identify the influence of cell shape anisotropy stochastics, an idealized foam mesostructural model is introduced as an array of periodically repeated Kelvin cells, which has been frequently used in the literature (see e.g. [60, 61, 62, 73]). \mathcal{R}^E and \mathcal{R}^σ of the idealized model for each Divinycell foam grade can be determined by substituting the overall cell shape anisotropy \mathcal{R} (see Table 2) into the present analytical model (52), which has been validated against numerical simulations (see Figure 15(b)). The results are reported in Figures 20(a) and (b), respectively (dark cyan and pink squares). It can be seen that the idealized model underestimates \mathcal{R}^E and \mathcal{R}^σ with respect to the tessellation-based models. In particular for \mathcal{R}^σ , the predictive deviation is $> 30\%$. This is likely due to the high sensitivity of compressive strength to mesostructural stochastics.

To unravel the idealized model predictive deviations in more detail, the individual cell mechanical anisotropy \mathcal{R}_v^E and \mathcal{R}_v^σ are computed by substituting the shape anisotropy \mathcal{R}_v (see Figures A.21(a) and (b)) into eq. (52). The corresponding probability density functions (PDF) for H100 and H200 are reported in Figures 20(c) and (d), respectively. Because of the stronger dependency on \mathcal{R}_v (see Figure 15(b)), \mathcal{R}_v^E exhibits a larger spread compared

with \mathcal{R}_v^σ . Furthermore, the five-number summary statistics of \mathcal{R}_v^E and \mathcal{R}_v^σ are indicated in Figures 20(a) and (b), respectively (dark cyan and pink windows). It can be seen that the upper quartile (top edge of the window) of \mathcal{R}_v^E closely represents \mathcal{R}^E of the tessellation-based models, while the upper bound (top black edge over the window) of \mathcal{R}_v^σ approximately represents \mathcal{R}^σ of the tessellation-based models. These observations suggest that the mechanical anisotropy, especially strength anisotropy, of a foam mesostructure with random cell shape anisotropy, is governed by the cells with relatively large shape anisotropy and cannot be simply correlated to the overall cell shape anisotropy.

Based on the comparative study above, it can be concluded that:

- The cell shape anisotropy stochastics have strong impacts on the resulting mechanical anisotropy, in particular strength anisotropy.
- The cell size and cell wall thickness stochastics play a rather secondary role.

A model without taking into account the cell shape anisotropy stochastics would apparently underestimate the mechanical anisotropy of realistic foams.

Besides, \mathcal{R}^E and \mathcal{R}^σ predicted by the reference analytical model, Sullivan model [34], are reported in Figures 20(a) and (b), respectively (light cyan and pink squares). It is found that the Sullivan model overestimates both \mathcal{R}^E and \mathcal{R}^σ with respect to the tessellation-based models. Especially for H200, the predictive deviations are $> 30\%$. Interestingly for H100, the Sullivan model demonstrates even better predictive capabilities than the present analytical model.

The Sullivan model seems to give reasonably good predictions. This is, however, a consequence of two sources of deviations compensating for each other. On one hand, introducing inappropriate mechanistic assumptions leads to that mechanical anisotropy is significantly overestimated (see Figure 15(b)). On the other hand, disregarding the cell shape anisotropy stochastics results in that mechanical anisotropy is apparently underestimated (see above detailed discussions for the present analytical model). Depending on the competition between the two sources of deviations, the predictive capabilities of the Sullivan model would largely vary from one case to another. This has been recognized in many studies for realistic foams (see e.g. [34, 35, 10, 36]), where the experimental uncertainties also play a role.

8. Conclusions

Focusing on closed-cell foams with a high cell face fraction and low relative density, a systematic numerical study has been performed to investigate the anisotropic compressive behavior, which takes into account cell shape anisotropy, cell structure and different mesostructural stochastics. The main findings are summarized:

- The anisotropic compressive properties of Divinycell foam H100 and H200 predicted by the tessellation-based models that include all the cell size, cell wall thickness and cell shape anisotropy stochastics, can closely represent the experimental results in [97, 98]. Yet, as a remark, there is a large inconsistency among the experimental data from different literature, calling for more attention to the experimental aspects.
- The cell wall membrane deformation dominates the initial elastic region, irrespective of the loading direction. Compared with this predominant deformation mechanism, the cell wall bending contribution is small at the early stage and becomes important only after foam yielding.
- The anisotropy of compressive properties is related to cell shape anisotropy through three pathways, cell load-bearing area fraction, cell wall buckling stress and cell wall inclination angle. The inclination angle has crucial impacts on the resulting mechanical anisotropy, in particular modulus anisotropy.

- The cell shape anisotropy stochastics strongly affect the anisotropy of compressive properties, in particular strength anisotropy. In contrast, the impacts of the cell size and cell wall thickness stochastics are much less important.
- The mechanistic assumptions introduced in the two widely used analytical models [32, 34] appear to be inappropriate at a high cell face fraction and low relative density. This becomes another key source of deviations besides different uncertainties in the real foam mesostructures and experiments, and explains why the predictive capabilities of these analytical models can sometimes be quite low (see e.g. [35, 36, 27, 9]).

Through quantitative analysis of the cell wall deformation behavior, this contribution confirms the dominant role of membrane deformation in the initial elastic region, as suggested in other studies (see e.g. [44, 45, 61]). The present findings on the impacts of cell shape anisotropy, cell structure and different mesostructural stochastics, provide deeper insights into how the anisotropic compressive properties are related to mesostructural features. The developed analytical models that describe the relationships between mechanical anisotropy and cell shape anisotropy, may provide new design guidelines for not only traditional foams, but also lattice structures consisting of regular cells (see e.g. [105, 106, 107]).

In realistic foams, cell walls tend to be thicker around the edges and thinner towards the face centers, and may undergo wavy distortions during the manufacturing process. Besides the stochastic variations of cell size, cell wall thickness and cell shape, there is likely a spread on individual cell elongation directions. Moreover, the cell wall plastic collapse becomes important upon a large applied strain, in particular to capture the plateau region observed at the macroscale. In addition, the strain rate effects and orientation effects of base materials may influence the anisotropic compressive behaviour. These aspects have not been considered here and will be investigated in the next steps.

Acknowledgements

This research was carried out under project numbers 2020-04526 and 2023-01937 in the framework of the Strategic Innovation Programme LIGHTer, funded by the Swedish Agency for Innovation Systems (Vinnova) and supported by the Swedish government.

Appendix A. Numerically realized mesostructural stochastics

The stochastic variations of different mesostructural features for the tessellation-based models introduced in Section 4, are elaborated in this appendix.

Detailed experimental characterization has been conducted in [5] for Diab Divinycell foam H100 and H200. Both three-dimensional (3D) and 2D images obtained using X-ray CT scan and scanning electron microscope (SEM), respectively, are analyzed. It is found that 3D and 2D measurements lead to similar distributions of cell equivalent diameter. However, cell wall thickness are largely overestimated with 3D measurements. Therefore, 2D measurements are adopted in the following.

The cell equivalent diameters d_v follow a log-normal distribution [5]:

$$f(d_v) = \frac{1}{d_v \sigma \sqrt{2\pi}} \exp\left(-\frac{(\ln d_v - \mu)^2}{2\sigma^2}\right), \quad (\text{A.1})$$

where μ and σ are the mean and standard deviation of $\ln d_v$, respectively. μ and σ can be related to the mean μ_d and standard deviation σ_d of d_v through:

$$\mu = \ln\left(\frac{\mu_d^2}{\sqrt{\mu_d^2 + \sigma_d^2}}\right), \quad \sigma^2 = \ln\left(1 + \frac{\sigma_d^2}{\mu_d^2}\right). \quad (\text{A.2})$$

The cell wall thickness t follows a gamma distribution [5]:

$$f(t) = \frac{1}{\Gamma\theta^\alpha} t^{\alpha-1} \exp\left(-\frac{t}{\theta}\right), \quad (\text{A.3})$$

where α and θ denote the shape and scale parameters, respectively; Γ is the gamma function, given by $\Gamma(\alpha) = \int_0^\infty x^{\alpha-1} \exp(x) dx$. α and θ can be related to the mean μ_t and standard deviation σ_t of t through:

$$\alpha = \frac{\mu_t^2}{\sigma_t^2}, \quad \theta = \frac{\sigma_t^2}{\mu_t}, \quad (\text{A.4})$$

Based on 2D measurements reported in [5], (μ_d, σ_d) and (μ_t, σ_t) for H100 and H200 are fitted, respectively, with the results listed in Table 2. No detailed measurements on individual cell shape anisotropy \mathcal{R}_v are provided in [5]. Therefore, only the overall cell shape anisotropy \mathcal{R} are given in Table 2.

Probability density functions (PDF) of different mesostructural features of the generated model set “StSt” for Divinycell foam H100 and H200, are compared to the prescribed ones in Figure A.21. An excellent agreement can be observed between the prescribed and numerically realized distributions, indicating that “StSt” can well approximate the real foam mesostructures. Notice that assigning an overall \mathcal{R} would still cause varying \mathcal{R}_v of individual cells, because of the cell shape irregularity naturally induced by Laguerre tessellation. As expected, the cell aspect ratios $\mathcal{R}_{v,31}$ and $\mathcal{R}_{v,32}$ are quite comparable, and both approximately follow a normal distribution (see Figures A.21(a) and (b)). This trend is in evidenced in more recent experimental measurements [89].

Appendix B. Influence of the RVE size and random realization

The particular choice of RVE size and random realization may affect the macroscale effective responses shown in Section 7, and is thus examined in this appendix.

The tessellation-based model “StSt” for Divinycell foam H100 is focused on as one example. Four different choices of the RVE size L_i are investigated, tiny 0.90 [mm], small 1.15 [mm], medium 1.50 [mm] and large 1.75 [mm]. Using the same random seed, RVE models consisting of 26, 54, 119 and 189 cells, respectively, are generated. The resulting overall relative densities ρ/ρ_r are 0.0682, 0.0742, 0.0806 and 0.0835, respectively. The effective stresses $\hat{\mathbf{P}}$ of the four RVE models under compression in the foam rise (\vec{e}_3) direction are reported in Figure B.22(a). It can be seen that as the RVE size increases, the effective stress response tends to increase (see also e.g. [62, 9, 72]). This is likely because of the higher ρ/ρ_r associated with the larger RVE size. Nevertheless, the effective stress responses for the medium and large RVE sizes are almost the same. Interestingly, different RVE size choices lead to comparable cell wall buckling events, see the fractions N_c/N_w of buckled cell walls in Figure B.22(b). The “medium” size has been adopted in the present study.

Next, the sensitivity to the RVE random realization is investigated. Four different random seeds with the medium RVE size $L_i = 1.50$ [mm] are considered. It has been verified that the resulting ρ/ρ_r are almost the same. The corresponding effective responses and cell wall buckling events are reported in Figures B.23(a) and (b), respectively. It can be observed that different RVE random realizations deliver quite consistent results, especially the effective stress responses, which are visually almost indistinguishable. The random realization “1” has been adopted in the present study.

Similar findings have been confirmed for two transverse directions (\vec{e}_1/\vec{e}_2), which are thus not presented here.

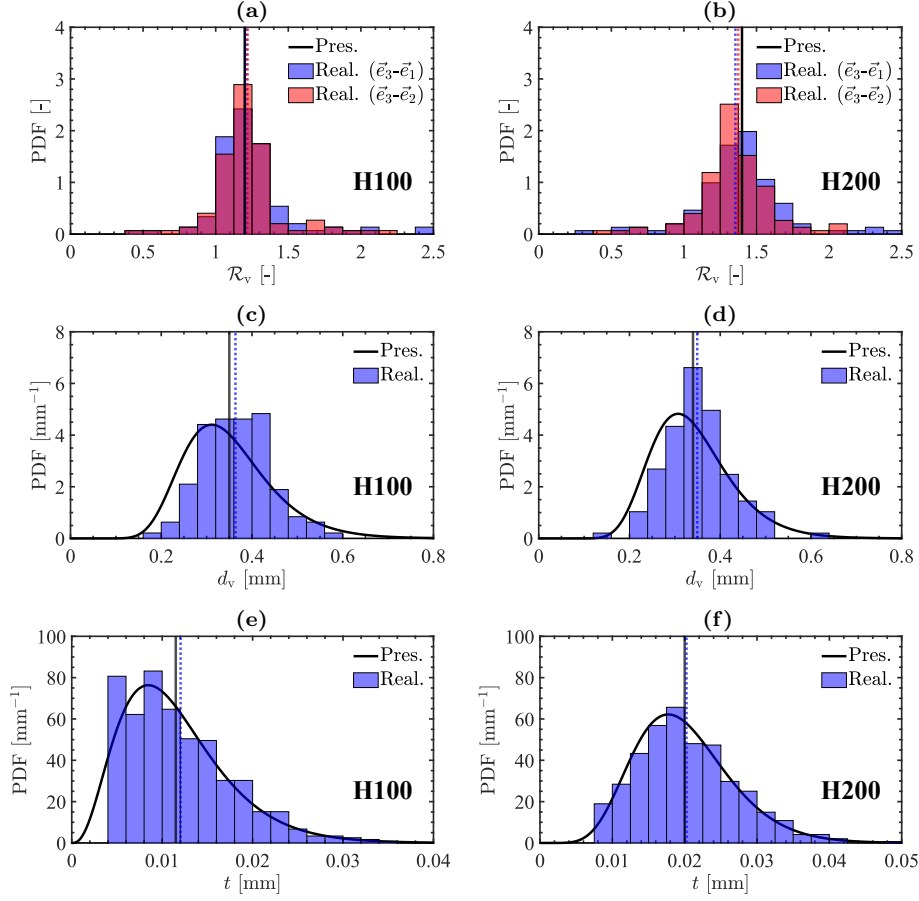


Figure A.21: Probability density functions (PDF) of different mesostructural features of the tessellation-based model set “StSt” for two Divinycell foam grades: (a-b) cell shape anisotropy, (c-d) cell equivalent diameter and (e-f) cell wall thickness. Comparison between the prescribed and numerically realized distributions is shown. The means of the prescribed and numerically realized distributions are indicated by the solid and dashed vertical lines, respectively.

Appendix C. Reference analytical models

Two reference analytical models assessed in Sections 6 and 7 for the predictions of foam mechanical anisotropy under compression, are detailed in this appendix.

The first one is the Gibson-Ashby model [32], which is derived by adopting a rectangular parallelepiped cell structure. The cell edge bending deformation, accompanied by the face membrane deformation along the direction perpendicular to the compressive loading, is assumed to govern the initial elastic region. The cell wall plastic collapse is assumed to be the leading failure mode. The mechanical anisotropy \mathcal{R}^E and \mathcal{R}^σ are expressed in terms of shape anisotropy \mathcal{R} as:

$$\mathcal{R}^E = \phi \frac{2\mathcal{R}^2}{1 + \mathcal{R}^{-3}} + (1 - \phi) \frac{2\mathcal{R}}{1 + \mathcal{R}^{-1}}, \quad (\text{C.1a})$$

$$\mathcal{R}^\sigma = \frac{2\mathcal{R}}{1 + \mathcal{R}^{-1}}, \quad (\text{C.1b})$$

where ϕ denotes the cell edge fraction. Note, that the physical interpretation of ϕ has been relaxed, which is instead treated as a fitting parameter in the Gibson-Ashby model.

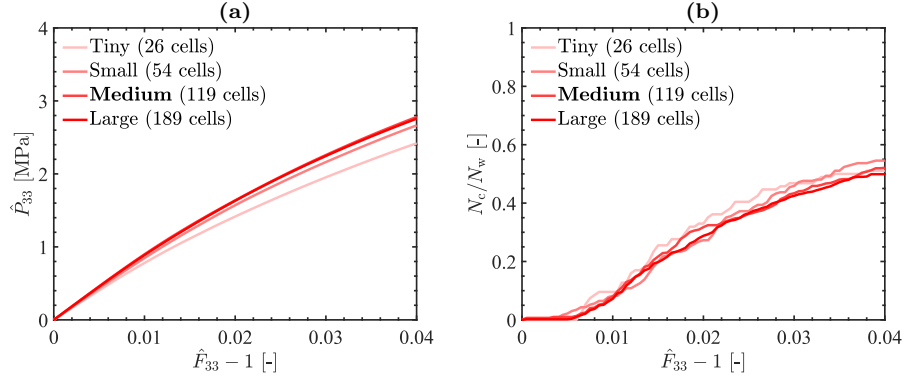


Figure B.22: (a) Effective stresses and (b) fractions of buckled cell walls versus applied strain of the tessellation-based models “StSt” H100 for different RVE sizes, under uniaxial compression in the foam rise (\vec{e}_3) direction. The curves for medium and large RVE sizes in (a) are nearly overlapping.

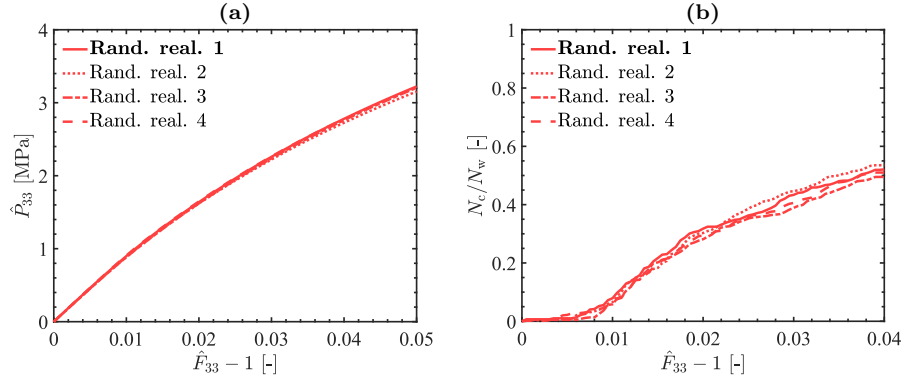


Figure B.23: (a) Effective stresses and (b) fractions of buckled cell walls versus applied strain of the tessellation-based models “StSt” H100 for different RVE random realizations, under uniaxial compression in the foam rise (\vec{e}_3) direction. The curves for random realizations “1” and “3” in (a) are nearly overlapping.

Interestingly, the fitted ϕ are found to be much higher than the experimental data for some closed-cell foams (see e.g. [108, 109, 110]).

For consistency with numerical simulations, $\phi = 0$ has been used in the present study. The results predicted using eq. C.1 are reported in Figure 15(a).

The second one is the Sullivan model [34], which is derived by adopting a (open-cell) Kelvin cell structure. The cell edge axial and bending deformations are both taken into account. The cell edge axial failure after reaching the base material ultimate strength is assumed to be the foam failure mechanism. The resulting \mathcal{R}^E and \mathcal{R}^σ are expressed as:

$$\mathcal{R}^E = \frac{\mathcal{R}^2}{4} \frac{\mathcal{A}_1 \mathcal{A}_2}{\mathcal{A}_3} \quad (\text{C.2a})$$

$$\mathcal{R}^\sigma = \mathcal{R} \frac{\mathcal{B}_1 \mathcal{B}_2}{\mathcal{B}_3}, \quad (\text{C.2b})$$

with the intermediate terms

$$\mathcal{A}_1 = C_1 \left(2\tilde{Q}^2 \mathcal{R}^2 + \frac{64Q^3}{\mathcal{R}_1^{\frac{1}{2}}} \right), \quad (\text{C.3a})$$

$$\mathcal{A}_2 = \gamma C_2 \frac{8\tilde{Q}^3(32 + 4Q\mathcal{R}_1^{\frac{1}{2}})\mathcal{R}}{\mathcal{R}_1\mathcal{R}_2}, \quad (\text{C.3b})$$

$$\mathcal{A}_3 = 16C_1 + \gamma C_2 \frac{8\tilde{Q}^5\mathcal{R}^3}{\mathcal{R}_1\mathcal{R}_2}, \quad (\text{C.3c})$$

and

$$\mathcal{B}_1 = \sqrt{C_1}\tilde{Q}\mathcal{R}, \quad (\text{C.4a})$$

$$\mathcal{B}_2 = \sqrt{\gamma}C_3 \frac{16\sqrt{2}\tilde{Q}^{\frac{3}{2}}\mathcal{R}^{\frac{1}{2}}}{\mathcal{R}_1^{\frac{1}{2}}\mathcal{R}_2^{\frac{1}{2}}}, \quad (\text{C.4b})$$

$$\mathcal{B}_3 = 4\sqrt{C_1} + \sqrt{\gamma}C_3 \frac{4\sqrt{2}\tilde{Q}^{\frac{5}{2}}\mathcal{R}^{\frac{3}{2}}}{\mathcal{R}_1^{\frac{1}{2}}\mathcal{R}_2^{\frac{1}{2}}}, \quad (\text{C.4c})$$

respectively, where two additional ratios \mathcal{R}_1 and \mathcal{R}_2 have been introduced:

$$\mathcal{R}_1 = 16 + \tilde{Q}^2\mathcal{R}^2, \quad \mathcal{R}_2 = 4Q + 2(16 + \tilde{Q}^2\mathcal{R}^2)^{\frac{1}{2}}. \quad (\text{C.5})$$

Here, Q denotes a Kelvin cell shape parameter and $\tilde{Q} = 2 + \sqrt{2}Q$; $\gamma = \rho/\rho_r$ is the relative density; C_1 , C_2 and C_3 are three constants which characterize the cell edge cross-section shape.

Considering a standard Kelvin cell shape and three-cusp hypocycloid cross-section shape of cell edges, leads to $Q = \sqrt{2}$, and $C_1 = \sqrt{3} - \frac{\pi}{2}$, $C_2 = \frac{20\sqrt{3}-11\pi}{2\sqrt{3}-\pi}$ and $C_3 = \frac{60-11\sqrt{3}\pi}{24(\sqrt{3}-\frac{\pi}{2})}$ [34]. The results predicted using eq. C.2 are reported in Figures 15(b), 20(a) and 20(b).

References

- [1] B.H. Smith, S. Szyniszewski, J.F. Hajjar, B.W. Schafer, and S.R. Arwade. Steel foam for structures: A review of applications, manufacturing and material properties. *Journal of Constructional Steel Research*, 71:1–10, 2012. 1, 2
- [2] Y.L. Sun and Q.M. Li. Dynamic compressive behaviour of cellular materials: A review of phenomenon, mechanism and modelling. *International Journal of Impact Engineering*, 112:74–115, 2018. 1, 2
- [3] F. Rahimidehghan and W. Altenhof. Compressive behavior and deformation mechanisms of rigid polymeric foams: A review. *Composites Part B: Engineering*, 253:110513, 2023. 1, 2
- [4] Y. Mu, G. Yao, and H. Luo. Effect of cell shape anisotropy on the compressive behavior of closed-cell aluminum foams. *Materials & Design*, 31(3):1567–1569, 2010. 2, 3, 5
- [5] Y. Zhou, B. Xue, W. Zhang, and R. Wang. Prediction of bulk mechanical properties of PVC foam based on microscopic model: Part I-Microstructure characterization and generation algorithm. *Polymer Testing*, 117:107872, 2023. 2, 3, 14, 33, 34
- [6] W.Y. Jang, W.Y. Hsieh, C.C. Miao, and Y.C. Yen. Microstructure and mechanical properties of ALPORAS closed-cell aluminium foam. *Materials Characterization*, 107:228–238, 2015. 2, 13
- [7] Y. Tang, W. Zhang, X. Jiang, J. Zhao, W. Xie, and T. Chen. Experimental investigations on phenomenological constitutive model of closed-cell PVC foam considering the effects of density, strain rate and anisotropy. *Composites Part B: Engineering*, 238:109885, 2022. 2, 3, 5, 13, 14, 21

- [8] L.J. Gibson and M.F. Ashby. The mechanics of foams: basic results. In Cellular Solids, pages 175–234. Cambridge University Press, 1997. [2](#), [3](#), [29](#)
- [9] Y. Zhou, B. Xue, W. Zhang, and R. Wang. Prediction of bulk mechanical properties of PVC foam based on microscopic model: Part II-Material characterization and analytical formulae. Polymer Testing, 117:107846, 2023. [2](#), [3](#), [4](#), [5](#), [12](#), [15](#), [21](#), [26](#), [33](#), [34](#)
- [10] J. Andersons, M. Kirpluks, L. Stiebra, and U. Cabulis. Anisotropy of the stiffness and strength of rigid low-density closed-cell polyisocyanurate foams. Materials & Design, 92:836–845, 2016. [3](#), [4](#), [32](#)
- [11] P.J. Tan, S.R. Reid, J.J. Harrigan, Z. Zou, and S. Li. Dynamic compressive strength properties of aluminium foams. Part I-experimental data and observations. Journal of the Mechanics and Physics of Solids, 53(10):2174–2205, 2005. [3](#), [4](#)
- [12] D. Zenkert and M. Burman. Tension, compression and shear fatigue of a closed cell polymer foam. Composites Science and Technology, 69(6):785–792, 2009. [3](#), [4](#)
- [13] T.H. Kidd, S. Zhuang, and G. Ravichandran. In situ mechanical characterization during deformation of PVC polymeric foams using ultrasonics and digital image correlation. Mechanics of Materials, 55:82–88, 2012. [3](#), [4](#)
- [14] B. Koohbor, S. Ravindran, and A. Kidane. Effects of cell-wall instability and local failure on the response of closed-cell polymeric foams subjected to dynamic loading. Mechanics of Materials, 116:67–76, 2018. [3](#), [4](#)
- [15] Y. Duan, B. Du, X. Shi, B. Hou, and Y. Li. Quasi-static and dynamic compressive properties and deformation mechanisms of 3D printed polymeric cellular structures with Kelvin cells. International Journal of Impact Engineering, 132:103303, 2019. [3](#), [4](#)
- [16] A.H. Benouali, L. Froyen, T. Dillard, S. Forest, and F. N’guyen. Investigation on the influence of cell shape anisotropy on the mechanical performance of closed cell aluminium foams using micro-computed tomography. Journal of Materials Science, 40(22):5801–5811, 2005. [3](#)
- [17] H. Bafti and A. Habibolahzadeh. Compressive properties of aluminum foam produced by powder-Carbamide spacer route. Materials & Design, 52:404–411, 2013. [3](#)
- [18] Y. Cheng, Y. Li, X. Chen, X. Zhou, and N. Wang. Compressive properties and energy absorption of aluminum foams with a wide range of relative densities. Journal of Materials Engineering and Performance, 27(8):4016–4024, 2018. [3](#)
- [19] M.C. Saha, H. Mahfuz, U.K. Chakravarty, M. Uddin, Md. E. Kabir, and S. Jeelani. Effect of density, microstructure, and strain rate on compression behavior of polymeric foams. Materials Science and Engineering: A, 406(1-2):328–336, 2005. [3](#)
- [20] D.P. Mondal, M.D. Goel, and S. Das. Compressive deformation and energy absorption characteristics of closed cell aluminum-fly ash particle composite foam. Materials Science and Engineering: A, 507(1-2):102–109, 2009. [3](#)
- [21] C. Guo, T. Zou, C. Shi, X. Yang, N. Zhao, E. Liu, and C. He. Compressive properties and energy absorption of aluminum composite foams reinforced by in-situ generated MgAl₂O₄ whiskers. Materials Science and Engineering: A, 645:1–7, 2015. [3](#)

- [22] Y.W. Kim, Y.J. Jin, Y.S. Chun, I.H. Song, and H.D. Kim. A simple pressing route to closed-cell microcellular ceramics. Scripta Materialia, 53(8):921–925, 2005. [3](#)
- [23] A. Celzard, W. Zhao, A. Pizzi, and V. Fierro. Mechanical properties of tannin-based rigid foams undergoing compression. Materials Science and Engineering: A, 527(16-17):4438–4446, 2010. [3](#)
- [24] V.S. Deshpande and N.A. Fleck. Multi-axial yield behaviour of polymer foams. Acta Materialia, 49(10):1859–1866, 2001. [3](#), [5](#)
- [25] R. Edwin Raj and B.S.S. Daniel. Structural and compressive property correlation of closed-cell aluminum foam. Journal of Alloys and Compounds, 467(1-2):550–556, 2009. [3](#), [5](#)
- [26] E. Linul, N. Movahedi, and L. Marsavina. The temperature and anisotropy effect on compressive behavior of cylindrical closed-cell aluminum-alloy foams. Journal of Alloys and Compounds, 740:1172–1179, 2018. [3](#), [5](#)
- [27] Y. Liu, F. Rahimidehghan, and W. Altenhof. Anisotropic compressive behavior of rigid PVC foam at strain rates up to 200 s^{-1} . Polymer Testing, 91:106836, 2020. [3](#), [4](#), [5](#), [21](#), [26](#), [29](#), [31](#), [33](#)
- [28] A.R. Hamilton, O.T. Thomsen, L.A.O. Madaleno, L.R. Jensen, J.M. Rauhe, and R. Pyrz. Evaluation of the anisotropic mechanical properties of reinforced polyurethane foams. Composites Science and Technology, 87:210–217, 2013. [3](#)
- [29] M. Marvi-Mashhadi, C.S. Lopes, and J. LLorca. Effect of anisotropy on the mechanical properties of polyurethane foams: An experimental and numerical study. Mechanics of Materials, 124:143–154, 2018. [3](#), [5](#)
- [30] P. Li, Y.B. Guo, M.W. Zhou, and V.P.W. Shim. Response of anisotropic polyurethane foam to compression at different loading angles and strain rates. International Journal of Impact Engineering, 127:154–168, 2019. [3](#), [5](#)
- [31] E. Linul, L. Marsavina, T. Voiconi, and T. Sadowski. Study of factors influencing the mechanical properties of polyurethane foams under dynamic compression. Journal of Physics: Conference Series, 451:012002, 2013. [3](#)
- [32] L.J. Gibson and M.F. Ashby. The mechanics of foams: refinements. In Cellular Solids, pages 235–282. Cambridge University Press, 1997. [3](#), [4](#), [6](#), [24](#), [25](#), [26](#), [33](#), [35](#)
- [33] L. Gong, S. Kyriakides, and W.Y. Jang. Compressive response of open-cell foams. Part I: Morphology and elastic properties. International Journal of Solids and Structures, 42(5-6):1355–1379, 2005. [3](#), [4](#)
- [34] R.M. Sullivan, L.J. Ghosn, and B.A. Lerch. A general tetrakaidecahedron model for open-celled foams. International Journal of Solids and Structures, 45(6):1754–1765, 2008. [3](#), [4](#), [6](#), [25](#), [26](#), [31](#), [32](#), [33](#), [36](#), [37](#)
- [35] J.J. Espadas-Escalante and F. Avilés. Anisotropic compressive properties of multiwall carbon nanotube/polyurethane foams. Mechanics of Materials, 91:167–176, 2015. [4](#), [26](#), [32](#), [33](#)
- [36] L. Doyle, I. Weidlich, and M. Illguth. Anisotropy in polyurethane pre-insulated pipes. Polymers, 11(12):2074, 2019. [4](#), [26](#), [32](#), [33](#)

- [37] M.A. Kader, M.A. Islam, M. Saadatfar, P.J. Hazell, A.D. Brown, S. Ahmed, and J.P. Escobedo. Macro and micro collapse mechanisms of closed-cell aluminium foams during quasi-static compression. Materials & Design, 118:11–21, 2017. [4](#), [13](#)
- [38] P. Poapongsakorn and C. Kanchanomai. Time-dependent deformation of closed-cell PVC foam. Journal of Cellular Plastics, 47(4):323–336, 2011. [4](#)
- [39] D.D. Luong, D. Pinisetty, and N. Gupta. Compressive properties of closed-cell polyvinyl chloride foams at low and high strain rates: Experimental investigation and critical review of state of the art. Composites Part B: Engineering, 44(1):403–416, 2013. [4](#)
- [40] F. Concas, S. Diebels, and A. Jung. Multiaxial failure surface of PVC foams and monitoring of deformation bands by three-dimensional digital image correlation. Journal of the Mechanics and Physics of Solids, 130:195–215, 2019. [4](#), [13](#)
- [41] D.S. Bolintineanu, R. Waymel, H. Collis, K.N. Long, E.C. Quintana, and S.L.B. Kramer. Anisotropy evolution of elastomeric foams during uniaxial compression measured via in-situ X-ray computed tomography. Materialia, 18:101112, 2021. [4](#)
- [42] H.W. Chai, Z.L. Xie, X.H. Xiao, H.L. Xie, J.Y. Huang, and S.N. Luo. Microstructural characterization and constitutive modeling of deformation of closed-cell foams based on in situ x-ray tomography. International Journal of Plasticity, 131:102730, 2020. [4](#), [5](#), [13](#), [23](#)
- [43] S. Santosa and T. Wierzbicki. On the modeling of crush behavior of a closed-cell aluminum foam structure. Journal of the Mechanics and Physics of Solids, 46(4):645–669, 1998. [4](#), [13](#)
- [44] A.E. Simone and L.J. Gibson. Effects of solid distribution on the stiffness and strength of metallic foams. Acta Materialia, 46(6):2139–2150, 1998. [4](#), [20](#), [33](#)
- [45] J.L. Grenestedt and F. Bassinet. Influence of cell wall thickness variations on elastic stiffness of closed-cell cellular solids. International Journal of Mechanical Sciences, 42(7):1327–1338, 2000. [4](#), [20](#), [33](#)
- [46] M. De Giorgi, A. Carofalo, V. Dattoma, R. Nobile, and F. Palano. Aluminium foams structural modelling. Computers & Structures, 88(1-2):25–35, 2010. [4](#)
- [47] E. Sadek and N.A. Fouad. Finite element modeling of compression behavior of extruded polystyrene foam using X-ray tomography. Journal of Cellular Plastics, 49(2):161–191, 2013. [4](#), [13](#)
- [48] Y. Chen, R. Das, M. Battley, and Z. Xu. Compressive and shear strengths of the ductile closed-cell Kelvin and Weaire-Phelan foams along the lattice direction [100]. Thin-Walled Structures, 132:237–249, 2018. [4](#), [10](#)
- [49] R. Shakibanezhad, M. Sadighi, and R. Hedayati. Numerical and experimental study of quasi-static loading of aluminum closed-cell foams using weaire-phelan and kelvin tessellations. Transport in Porous Media, 142(1-2):229–248, 2022. [4](#)
- [50] J. Carlsson, V.S. Deshpande, and N.A. Fleck. The compressive response of the filled Kelvin foam. European Journal of Mechanics - A/Solids, 104:105018, 2024. [4](#), [13](#)
- [51] O. Caty, E. Maire, S. Youssef, and R. Bouchet. Modeling the properties of closed-cell cellular materials from tomography images using finite shell elements. Acta Materialia, 56(19):5524–5534, 2008. [4](#)

- [52] I. Jeon, T. Asahina, K.J. Kang, S. Im, and T.. Lu. Finite element simulation of the plastic collapse of closed-cell aluminum foams with X-ray computed tomography. Mechanics of Materials, 42(3):227–236, 2010. [4](#)
- [53] M.A. Sulong, M. Taherishargh, I.V. Belova, G.E. Murch, and T. Fiedler. On the mechanical anisotropy of the compressive properties of aluminium perlite syntactic foam. Computational Materials Science, 109:258–265, 2015. [4](#)
- [54] K. Natesaiyer, C. Chan, S. Sinha-Ray, D. Song, C.L. Lin, J.D. Miller, E.J. Garboczi, and A.M. Forster. X-ray CT imaging and finite element computations of the elastic properties of a rigid organic foam compared to experimental measurements: insights into foam variability. Journal of Materials Science, 50(11):4012–4024, 2015. [4](#)
- [55] Y. Sun, X. Zhang, Z. Shao, and Q.M. Li. Image-based correlation between the meso-scale structure and deformation of closed-cell foam. Materials Science and Engineering: A, 688:27–39, 2017. [4](#)
- [56] Y. Chen, R. Das, and M. Battley. Finite element analysis of the compressive and shear responses of structural foams using computed tomography. Composite Structures, 159:784–799, 2017. [4](#)
- [57] S. Talebi, M. Sadighi, and M.M. Aghdam. Numerical and experimental analysis of the closed-cell aluminium foam under low velocity impact using computerized tomography technique. Acta Mechanica Sinica, 35(1):144–155, 2019. [4](#)
- [58] A. Ghazi, P. Berke, K. Ehab Moustafa Kamel, B. Sonon, C. Tiago, and T.J. Massart. Multiscale computational modelling of closed cell metallic foams with detailed microstructural morphological control. International Journal of Engineering Science, 143:92–114, 2019. [4](#)
- [59] A. Ghazi, C. Tiago, B. Sonon, P. Berke, and T.J. Massart. Efficient computational modelling of closed cell metallic foams using a morphologically controlled shell geometry. International Journal of Mechanical Sciences, 168:105298, 2020. [4](#)
- [60] Y. Song, Z. Wang, L. Zhao, and J. Luo. Dynamic crushing behavior of 3D closed-cell foams based on Voronoi random model. Materials & Design, 31(9):4281–4289, 2010. [4](#), [31](#)
- [61] X. Shi, S. Liu, H. Nie, G. Lu, and Y. Li. Study of cell irregularity effects on the compression of closed-cell foams. International Journal of Mechanical Sciences, 135:215–225, 2018. [4](#), [5](#), [20](#), [30](#), [31](#), [33](#)
- [62] B. Vengatachalam, L.H. Poh, Z.S. Liu, Q.H. Qin, and S. Swaddiwudhipong. Three dimensional modelling of closed-cell aluminium foams with predictive macroscopic behaviour. Mechanics of Materials, 136:103067, 2019. [4](#), [5](#), [12](#), [30](#), [31](#), [34](#)
- [63] A.P. Roberts and E.J. Garboczi. Elastic moduli of model random three-dimensional closed-cell cellular solids. Acta Materialia, 49(2):189–197, 2001. [4](#)
- [64] J. Köll and S. Hallström. Elastic properties of equilibrium foams. Acta Materialia, 113:11–18, 2016. [4](#)
- [65] Y. Chen, R. Das, and M. Battley. Effects of cell size and cell wall thickness variations on the stiffness of closed-cell foams. International Journal of Solids and Structures, 52:150–164, 2015. [5](#), [12](#), [29](#)

- [66] Y. Chen, R. Das, and M. Battley. Effects of cell size and cell wall thickness variations on the strength of closed-cell foams. International Journal of Engineering Science, 120:220–240, 2017. [5](#), [29](#)
- [67] B.Y. Su, C.M. Huang, H. Sheng, and W.Y. Jang. The effect of cell-size dispersity on the mechanical properties of closed-cell aluminum foam. Materials Characterization, 135:203–213, 2018. [5](#)
- [68] T.M.J. Gebhart, Di. Jehnichen, R. Koschichow, M. Müller, M. Göbel, V. Geske, M. Stegelmann, and M. Gude. Multi-scale modelling approach to homogenise the mechanical properties of polymeric closed-cell bead foams. International Journal of Engineering Science, 145:103168, 2019. [5](#)
- [69] M. Marvi-Mashhadi, C.S. Lopes, and J. LLorca. High fidelity simulation of the mechanical behavior of closed-cell polyurethane foams. Journal of the Mechanics and Physics of Solids, 135:103814, 2020. [5](#)
- [70] B.Y. Su and W.Y. Jang. The microstructure characterization and elastic properties of closed-cell foams. International Journal of Solids and Structures, 257:111700, 2022. [5](#)
- [71] A. Hössinger-Kalteis, M. Reiter, M. Jerabek, and Z. Major. Application of computed tomography data-based modelling technique for polymeric low density foams, Part A: Model development. Journal of Cellular Plastics, 58(3):429–448, 2022. [5](#)
- [72] Y. Ding, X. Zhou, J. Wang, Y. Feng, J. Tang, N. Shang, S. Xin, Xi. Jian, M. Gude, and J. Xu. A sophisticated periodic micro-model for closed-cell foam based on centroidal constraint and capacity constraint. Composite Structures, 303:116175, 2023. [5](#), [10](#), [34](#)
- [73] P. Gahlen and M. Stommel. Modeling of the local anisotropic mechanical foam properties in polyisocyanurate metal panels using mesoscale FEM simulations. International Journal of Solids and Structures, 244-245:111595, 2022. [5](#), [10](#), [31](#)
- [74] P. Gahlen and M. Stommel. Multiscale approach to determine the anisotropic mechanical properties of polyisocyanurate metal panels using FEM simulations. Mechanics of Materials, 174:104475, 2022. [5](#)
- [75] X. Huo, Z. Jiang, Q. Luo, Q. Li, and G. Sun. Mechanical characterization and numerical modeling on the yield and fracture behaviors of polymethacrylimide (PMI) foam materials. International Journal of Mechanical Sciences, 218:107033, 2022. [5](#)
- [76] M. Ostoja-Starzewski. Material spatial randomness: From statistical to representative volume element. Probabilistic Engineering Mechanics, 21(2):112–132, 2006. [5](#)
- [77] E. Reissner and Y. Stavsky. Bending and stretching of certain types of heterogeneous aeolotropic elastic plates. Journal of Applied Mechanics, 28(3):402–408, 1961. [6](#)
- [78] E.M.B. Campello, P.M. Pimenta, and P. Wriggers. A triangular finite shell element based on a fully nonlinear shell formulation. Computational Mechanics, 31(6):505–518, 2003. [6](#), [9](#), [15](#)
- [79] N.P. van Dijk. Formulation and implementation of stress-driven and/or strain-driven computational homogenization for finite strain. International Journal for Numerical Methods in Engineering, 107(12):1009–1028, 2016. [6](#), [11](#)
- [80] M.A. Saadat and D. Durville. A mixed stress-strain driven computational homogenization of spiral strands. Computers & Structures, 279:106981, 2023. [6](#), [11](#)

- [81] C. Larsson, F. Larsson, J. Xu, K. Runesson, and L.E. Asp. Effects of lithium insertion induced swelling of a structural battery negative electrode. Composites Science and Technology, 244:110299, 2023. [6](#), [11](#)
- [82] E.W.C. Coenen, V.G. Kouznetsova, and M.G.D. Geers. Computational homogenization for heterogeneous thin sheets. International Journal for Numerical Methods in Engineering, 83(8-9):1180–1205, 2010. [7](#)
- [83] L. Liu, A. Sridhar, M.G.D. Geers, and V.G. Kouznetsova. Computational homogenization of locally resonant acoustic metamaterial panels towards enriched continuum beam/shell structures. Computer Methods in Applied Mechanics and Engineering, 387:114161, 2021. [7](#)
- [84] V.G. Kouznetsova, W.A.M. Brekelmans, and F.P.T. Baaijens. An approach to micro-macro modeling of heterogeneous materials. Computational Mechanics, 27(1):37–48, 2001. [9](#), [11](#)
- [85] C. Miehe. Strain-driven homogenization of inelastic microstructures and composites based on an incremental variational formulation. International Journal for Numerical Methods in Engineering, 55(11):1285–1322, 2002. [9](#), [11](#), [15](#)
- [86] R. Hill. Elastic properties of reinforced solids: Some theoretical principles. Journal of the Mechanics and Physics of Solids, 11(5):357–372, 1963. [11](#)
- [87] M. Alkhader and M. Vural. The partition of elastic strain energy in solid foams and lattice structures. Acta Materialia, 57(8):2429–2439, 2009. [12](#)
- [88] J. Ding, Q. Ma, X. Li, L. Zhang, H. Yang, S. Qu, M.Y. Wang, W. Zhai, H. Gao, and X. Song. Imperfection-enabled strengthening of ultra-lightweight lattice materials. Advanced Science, 2024. [12](#)
- [89] J.W. Skeens and S. Kyriakides. Crushing of a closed-cell polymeric foam under triaxial loading. International Journal of Solids and Structures, 291:112686, 2024. [13](#), [14](#), [34](#)
- [90] R. Quey, A. Villani, and C. Maurice. Nearly uniform sampling of crystal orientations. Journal of Applied Crystallography, 51(4):1162–1173, 2018. [14](#)
- [91] Technical Data Divinycell H. Technical report, Diab Group, 2023. [14](#)
- [92] C. Geuzaine and J.-F. Remacle. Gmsh: A 3-D finite element mesh generator with built-in pre- and post-processing facilities. International Journal for Numerical Methods in Engineering, 79(11):1309–1331, 2009. [14](#)
- [93] T. Helfer, J. Bleyer, T. Frondelius, I. Yashchuk, T. Nagel, and D. Naumov. The MFrontGenericInterfaceSupport project. Journal of Open Source Software, 5(48):2003, 2020. [15](#), [16](#)
- [94] A. Logg, K.-A. Mardal, and G. Wells. Automated Solution of Differential Equations by the Finite Element Method. Springer Science & Business Media, 2012. [16](#)
- [95] J. Bleyer. Numerical Tours of Computational Mechanics with FEniCS. Zenodo, 2018. [16](#)
- [96] G. Gerard and H. Becker. Handbook of structural stability Part I: Buckling of flat plates. Technical report, New York University, 1957. [22](#), [24](#)

- [97] M. Shafiq, R.S. Ayyagari, M. Ehaab, and M. Vural. Multiaxial yield surface of transversely isotropic foams: Part II—Experimental. Journal of the Mechanics and Physics of Solids, 76:224–236, 2015. [27](#), [28](#), [29](#), [30](#), [31](#), [32](#)
- [98] M.F. Funari, S. Spadea, P. Lonetti, and P.B. Lourenço. On the elastic and mixed-mode fracture properties of PVC foam. Theoretical and Applied Fracture Mechanics, 112:102924, 2021. [27](#), [28](#), [29](#), [30](#), [31](#), [32](#)
- [99] S. Zhang, J.M. Dulieu-Barton, R.K. Fruehmann, and O.T. Thomsen. A methodology for obtaining material properties of polymeric foam at elevated temperatures. Experimental Mechanics, 52(1):3–15, 2012. [29](#), [31](#)
- [100] S.T. Taher, O.T. Thomsen, J.M. Dulieu-Barton, and S. Zhang. Determination of mechanical properties of PVC foam using a modified Arcan fixture. Composites Part A: Applied Science and Manufacturing, 43(10):1698–1708, 2012. [29](#), [31](#)
- [101] L. Chen and M.S. Hoo Fatt. Transversely isotropic mechanical properties of PVC foam under cyclic loading. Journal of Materials Science, 48(19):6786–6796, 2013. [29](#), [31](#)
- [102] X. Tong, M.S. Hoo Fatt, and A.R. Vedire. A new crushable foam model for polymer-foam core sandwich structures. International Journal of Crashworthiness, 27(5):1460–1480, 2022. [29](#), [31](#)
- [103] M.S. Hoo Fatt and A.R. Vedire. Mechanical properties of marine polymer foams in the arctic environment. Marine Structures, 86:103308, 2022. [29](#), [31](#)
- [104] J. Magliaro, F. Rahimidehgolan, P. Mohammadkhani, W. Altenhof, and A.T. Alpas. Modular energy absorbing capabilities achieved with compounded deformation mechanisms in composite AA6061-T6/PVC foam structures. Acta Mechanica, 234(9):4217–4258, 2023. [29](#), [31](#)
- [105] J.B. Berger, H.N.G. Wadley, and R.M. McMeeking. Mechanical metamaterials at the theoretical limit of isotropic elastic stiffness. Nature, 543(7646):533–537, 2017. [33](#)
- [106] T. Tancogne-Dejean, M. Diamantopoulou, M.B. Gorji, C. Bonatti, and D. Mohr. 3D plate-lattices: an emerging class of low-density metamaterial exhibiting optimal isotropic stiffness. Advanced Materials, 30(45), 2018. [33](#)
- [107] H. Guo and J. Zhang. Performance-oriented and deformation-constrained dual-topology metamaterial with high-stress uniformity and extraordinary plastic property. Advanced Materials, 2024. [33](#)
- [108] N.J. Mills and H.X. Zhu. The high strain compression of closed-cell polymer foams. Journal of the Mechanics and Physics of Solids, 47(3):669–695, 1999. [36](#)
- [109] O. Almanza, M.A. Rodriguez-Perez, and J.A. de Saja. The microstructure of polyethylene foams produced by a nitrogen solution process. Polymer, 42(16):7117–7126, 2001. [36](#)
- [110] N.J. Mills, R. Stämpfli, F. Marone, and P.A. Brühwiler. Finite element micromechanics model of impact compression of closed-cell polymer foams. International Journal of Solids and Structures, 46(3-4):677–697, 2009. [36](#)